

The impact of snow nitrate photolysis on boundary layer chemistry and the recycling and redistribution of reactive nitrogen across Antarctica in a global chemical transport model

Zatko, M.C.¹, Geng, L.¹, Alexander, B.¹, Sofen, E.D.², Klein, K.³

¹Department of Atmospheric Sciences, University of Washington, Seattle, United States

²Department of Chemistry, University of York, York, United Kingdom

³Division of Glaciology, Alfred Wegener Institute Helmholtz Centre for Polar and Marine Research, Bremerhaven, Germany

Correspondence to Becky Alexander (beckya@uw.edu)

1 **Abstract**

2 The formation and recycling of reactive nitrogen (NO, NO₂, HONO) at the air-snow
3 interface has implications for air quality and the oxidation capacity of the atmosphere in
4 snow-covered regions. Nitrate (NO₃⁻) photolysis in snow provides a source of oxidants
5 (e.g., hydroxyl radical) and oxidant precursors (e.g., nitrogen oxides) to the overlying
6 boundary layer, and alters the concentration and isotopic (e.g., δ¹⁵N) signature of NO₃⁻
7 preserved in ice cores. We have incorporated the photolysis of Antarctic snow NO₃⁻ into
8 a global chemical transport model (GEOS-Chem) to examine the implications of snow
9 NO₃⁻ photolysis for boundary layer chemistry, the recycling and redistribution of reactive
10 nitrogen across the Antarctic continent, and the preservation of ice-core NO₃⁻ in Antarctic
11 ice cores. This modeling framework uses an idealized snowpack that accounts for the
12 spatial variability in parameters that influence snow NO₃⁻ photolysis. The goal of this
13 research is to investigate the potential spatial variability of snow-sourced NO_x fluxes
14 along with the recycling, loss, and areal redistribution of nitrogen across Antarctica,
15 which is an environment in which observations of these parameters over large spatial
16 scales are difficult to obtain. The calculated potential fluxes of snow-sourced NO_x in
17 Antarctica range from 0.5 × 10⁸ to 7.8 × 10⁸ molec cm⁻² s⁻¹ and calculated e-folding depths
18 of UV actinic flux in snowpack range from 24 to 69 cm. Snow-sourced NO_x increases
19 mean austral summer boundary layer mixing ratios of total nitrate (HNO₃+NO₃⁻), NO_x,
20 OH, and O₃ in Antarctica by a factor of up to 32, 38, 7, and 2, respectively, in the model.
21 Model results also suggest that NO₃⁻ can be recycled between the air and snow multiple
22 times and that NO₃⁻ can remain in the snow photic zone for at least 7.5 years on the East
23 Antarctic plateau. The fraction of photolysis-driven loss of NO₃⁻ from the snow is
24 roughly -0.99 on the East Antarctic plateau, while areas of wind convergence (e.g., over
25 the Ronne Ice Shelf) have a net gain of NO₃⁻ due to redistribution of snow-sourced
26 reactive nitrogen across the Antarctic continent. The modeled enrichment in ice-core
27 δ¹⁵N(NO₃⁻) due to photolysis-driven loss of snow NO₃⁻ ranges from 0‰ to 363‰, with
28 the largest enrichments on the East Antarctic plateau. There is a strong relationship
29 between the degree of photolysis-driven loss of snow NO₃⁻ and the degree of nitrogen
30 recycling between the air and snow in regions of Antarctica with a snow accumulation
31 rate greater than 85 kg m⁻² a⁻¹ in the present day. This modeling framework study is also
32 used to perform a variety of sensitivity studies to highlight the largest uncertainties in our
33 ability to model these processes in order to guide future lab and field campaigns.

34

35

36

37

38

39

40

41

42

43

44

45

46

47 **1. Introduction**
 48 Nitrogen oxides ($\text{NO}_x = \text{NO} + \text{NO}_2$) emitted from fossil fuel combustion, biomass burning,
 49 soil microbial activity, and lightning have adverse respiratory effects, contribute to the
 50 formation of atmospheric acidity, and are a key ingredient in tropospheric oxidant cycling
 51 leading to the formation of ground-level ozone (O_3). Ozone also has adverse respiratory
 52 effects, is an effective greenhouse gas [UNEP, 2011], and its photolysis dominates
 53 hydroxyl radical (OH) production in much of the troposphere [Thompson, 1992].
 54 Oxidation to form nitrate ($\text{HNO}_3/\text{NO}_3^-$) is the main sink for NO_x in the troposphere
 55 [Logan, 1983], and the lifetime of NO_x against oxidation to nitrate is 1-3 days in polar
 56 regions [Levy *et al.*, 1999]. NO_3^- is lost from the atmosphere through dry and wet
 57 deposition to the Earth's surface, and has an atmospheric lifetime of roughly 5 days [Xu
 58 and Penner, 2012]. In Antarctica, NO_3^- deposited to the snowpack originates from both
 59 the troposphere (e.g., long-range transport) [Lee *et al.*, 2014] and stratosphere [Frey *et*
 60 *al.*, 2009, Savarino *et al.*, 2007]. In snow-covered regions, the deposition of NO_3^- is not a
 61 permanent sink for NO_x , as the photolysis of snow NO_3^- returns reactive nitrogen
 62 ($\text{N}_r = \text{NO}_x, \text{HONO}$) back to the atmosphere, with implications for other oxidants such as
 63 OH and ozone [Domine and Shepson, 2002].
 64

65 Snow photochemistry significantly influences boundary layer chemistry and plays an
 66 important role in oxidant production and cycling, especially in pristine regions, such as
 67 Antarctica [Bloss *et al.*, 2007, Chen *et al.*, 2004, Grannas *et al.*, 2007, Helmig *et al.*,
 68 2008]. Snow photochemistry may have more widespread impacts since up to 40% of land
 69 on Earth is snow-covered at a given time [Grannas *et al.*, 2007]. NO_3^- is not the only
 70 photochemically-active species in snow. The photolysis of nitrite (NO_2^-) in snow and the
 71 photolysis of snow-sourced formaldehyde (CH_2O), nitrous acid (HONO), and hydrogen
 72 peroxide (H_2O_2) provide additional sources of N_r and OH to the boundary layer. Bromine
 73 (Br_2) is also produced in the snow via reactions involving bromide (Br^-),
 74 photochemically-active species (e.g., NO_3^-), and photochemically-produced species (e.g.,
 75 OH) within snow grains [Pratt *et al.*, 2013].
 76

77 In snow, NO_3^- photolysis likely occurs in the liquid-like region (LLR) on the surface of
 78 ice grains, in cracks between ice grains, or in brine pockets embedded within ice grains
 79 [Domine *et al.*, 2013]. There are two channels for NO_3^- photolysis at wavelengths
 80 ($\lambda = 290-345 \text{ nm}$). In the aqueous phase, NO_3^- can photolyze to produce NO_2 and OH (E1),
 81 or produce NO_2^- and $\text{O}({}^3\text{P})$ (E2), but E1 is the dominant pathway [Grannas *et al.*, 2007,
 82 Mack and Bolton, 1999, Meusinger *et al.*, 2014].
 83

84 $\text{NO}_3^-(\text{aq}) + \text{hv}(\text{+H}^+) \rightarrow \text{NO}_2(\text{aq}) + \text{OH}(\text{aq}),$ E1
 85 $\text{NO}_3^-(\text{aq}) + \text{hv} \rightarrow \text{NO}_2^-(\text{aq}) + \text{O}({}^3\text{P})(\text{aq}),$ E2
 86

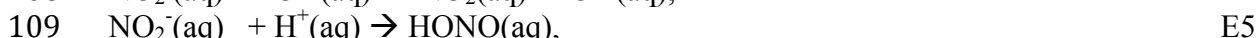
87 The aqueous phase NO_2 produced in E1 is can be transferred to the gas phase and
 88 subsequently transported into the interstitial air [Boxe *et al.*, 2005] and then released to
 89 the atmosphere. The quantum yield (ϕ) in E1 is strongly influenced by the location of
 90 NO_3^- in an ice grain. Chu and Anastasio [2003] froze NO_3^- -doped water in the lab and
 91 measured the quantum yield for E1 (0.003 molec photon $^{-1}$ at T=253K) as frozen ice
 92 grains were exposed to ultraviolet (UV) radiation. Zhu *et al.* [2010] deposited HNO_3 on

93 an ice film and measured ϕ for E1 (0.6 molec photon⁻¹ at T=253K), as the frozen surface
94 was irradiated with UV radiation. In a recent study by Meusinger et al. [2014], $\phi=0.003-$
95 0.44 molec photon⁻¹ for E1, which nearly spans the full range of previously reported
96 quantum yields. Results from Meusinger et al. [2014] suggest that ϕ is dependent on the
97 length of time that snow is exposed to UV radiation, as well as the location of NO₃⁻ in the
98 ice grain. Meusinger et al. [2014] suggest that two photochemical domains of NO₃⁻ exist:
99 photolabile NO₃⁻ and NO₃⁻ buried within the ice grain. The NO_x produced from the
100 photolysis of photolabile NO₃⁻ can escape the ice grain, while the NO_x produced from the
101 photolysis of buried NO₃⁻ is likely to undergo recombination chemistry within the snow
102 grain, thus lowering the quantum yield of NO_x for NO₃⁻ photolysis.

103

104 The NO₂⁻ produced in E2 is quickly photolyzed at longer wavelengths ($\lambda=290-390$ nm) in
105 the LLR or can react with OH or H⁺ in the LLR to produce N_r [Grannas et al., 2007]:

106



110

111 HONO produced in E5 can rapidly photolyze to produce NO and OH in the interstitial air
112 or the atmospheric boundary layer [Anastasio and Chu, 2009]. Reactions involving NO₂⁻
113 are intermediate reactions for NO₃⁻ photolysis because NO₃⁻ photolysis is required for
114 NO₂⁻ formation and the end products of E1-E5 are all N_r. Once emitted, NO₂ and NO are
115 efficiently transported to the overlying atmosphere via windpumping [Zatko et al., 2013]
116 and enter into rapid NO_x-cycling reactions. In the atmosphere, the relative abundance of
117 NO and NO₂ will be determined by local atmospheric conditions, specifically oxidant
118 concentrations (e.g., O₃, HO₂, RO₂, BrO, and ClO) [Frey et al., 2013]. The snow-sourced
119 NO_x is then re-oxidized to HNO₃ via E6 under sunlit conditions.

120



122

123 The HNO₃ produced in E6 can undergo wet or dry deposition to the snow surface [Dibb
124 et al., 2004] within a day [Slusher et al., 2002, Wang et al., 2008]. Evidence for HNO₃
125 re-deposition is seen in the snow NO₃⁻ concentration profile at many polar locations,
126 where NO₃⁻ concentrations are at least an order of magnitude higher in the top two
127 centimeters (cm) of snow compared to NO₃⁻ concentrations below [Dibb et al., 2004,
128 Frey et al., 2009, Mayewski and Legrand, 1990, Rothlisberger et al., 2000]. Once HNO₃
129 is deposited back to the snow, it is available for photolysis again. NO₃⁻ can be recycled
130 multiple times between the boundary layer and the snow before burial below the photic
131 zone [Davis et al., 2008, Erbland et al., 2015].

132

133 The photolysis of snow NO₃⁻ and subsequent recycling between the air and snow alters
134 the concentration and isotopic (e.g., $\delta^{15}\text{N}$) signature of NO₃⁻ that is ultimately preserved
135 in polar ice sheets, which hampers the interpretation of ice-core NO₃⁻ records [Wolff et
136 al., 2008]. Such records have been sought to reconstruct the past history of the abundance
137 of NO_x in the atmosphere [Wolff, 1995]. It has also been suggested that the nitrogen
138 ($\delta^{15}\text{N}$) and oxygen ($\Delta^{17}\text{O} = \delta^{17}\text{O} - 0.52 \times \delta^{18}\text{O}$) isotopic composition of ice-core NO₃⁻ can

139 provide information on past variability in atmospheric NO_x sources and oxidant
140 abundances [e.g., *Alexander et al.*, 2004, *Hastings et al.*, 2005]. Different sources of NO_x
141 have different $\delta^{15}\text{N}$ signatures ($\sim -19\text{\textperthousand}$ to $25\text{\textperthousand}$, see summary in *Geng et al.*, 2014a),
142 giving ice-core $\delta^{15}\text{N}(\text{NO}_3^-)$ measurements the potential to track NO_x-source changes over
143 time. The oxygen-17 excess of NO₃⁻ ($\Delta^{17}\text{O}(\text{NO}_3^-)$) is determined mainly by the relative
144 abundance of the oxidants involved in NO_x cycling and conversion of NO₂ to NO₃⁻ (i.e.
145 O₃, HO₂, RO₂, OH), giving ice-core $\Delta^{17}\text{O}(\text{NO}_3^-)$ measurements the potential to track
146 variability in the relative abundance of these oxidants over time. However, $\delta^{15}\text{N}(\text{NO}_3^-)$
147 and $\Delta^{17}\text{O}(\text{NO}_3^-)$ in ice cores can also be influenced by post-depositional processing of
148 snow NO₃⁻ initiated by photolysis. In this study we focus on the impact of snow NO₃⁻
149 photolysis on ice-core $\delta^{15}\text{N}(\text{NO}_3^-)$.
150

151 Ice-core $\delta^{15}\text{N}(\text{NO}_3^-)$ values will be altered if there is photolysis-driven loss of NO₃⁻ from
152 the snow when snow-sourced NO_x is transported away from the site of primary
153 deposition. Nitrate photolysis in snow is associated with a large fractionation constant (ε)
154 of $-47.9\text{\textperthousand}$ [*Berhanu et al.*, 2014], providing the boundary layer with a source of NO_x that
155 is highly depleted in $\delta^{15}\text{N}$, leaving highly enriched $\delta^{15}\text{N}(\text{NO}_3^-)$ in the snow. In the
156 Weddell Sea, atmospheric $\delta^{15}\text{N}(\text{NO}_3^-)$ values are as low as $-40\text{\textperthousand}$, indicating transport of
157 snow-sourced NO_x from the continental interior [*Morin et al.*, 2009], while on the East
158 Antarctica plateau, snow $\delta^{15}\text{N}(\text{NO}_3^-)$ up to $480\text{\textperthousand}$ has been reported [*Blunier et al.*, 2005,
159 *Erblund et al.*, 2013, *Frey et al.*, 2009, *Shi et al.*, 2014], indicating net loss of NO₃⁻ driven
160 by photolysis. If snow-sourced NO_x is simply re-deposited back to the snow surface at
161 the site of emission, a vertical profile in $\delta^{15}\text{N}(\text{NO}_3^-)$ within the snow photic zone will
162 develop due to vertical redistribution of NO₃⁻ [*Erblund et al.*, 2013, *Frey et al.*, 2009];
163 however, the depth-integrated $\delta^{15}\text{N}(\text{NO}_3^-)$ will not be impacted, even with active
164 photolysis-driven recycling between the atmosphere and the snow. Enrichment in
165 $\delta^{15}\text{N}(\text{NO}_3^-)$ in ice cores requires photolysis-driven loss from snow combined with
166 atmospheric transport of the resulting NO_x. In addition to photolysis, ice-core $\delta^{15}\text{N}(\text{NO}_3^-)$
167 values are also influenced by evaporation of HNO₃ [*Mulvaney et al.*, 1998] from snow
168 and by atmospheric processing, such as NO_x cycling [*Freyer et al.*, 1993] and gas-particle
169 partitioning [*Heaton et al.*, 1997, *Geng et al.*, 2014a]; however, these impose a
170 fractionation in $\delta^{15}\text{N}(\text{NO}_3^-)$ at least an order of magnitude smaller than photolysis, and
171 are thus not able to explain the large enrichments in snow $\delta^{15}\text{N}(\text{NO}_3^-)$ observed on the
172 East Antarctic plateau [*Blunier et al.*, 2005, *Erblund et al.*, 2013, *Frey et al.*, 2009, *Shi et*
173 *al.*, 2014].
174

175 Here we incorporate a snowpack actinic flux parameterization used to calculate the
176 photolysis of snow NO₃⁻ into a global chemical transport model. The idealized Antarctic
177 ice sheet incorporated into GEOS-Chem has similar topography, climate, and weather as
178 the real Antarctic ice sheet, but is subject to assumptions about the chemical and physical
179 properties of the snow. The idealized snowpack in this modeling framework accounts for
180 the spatial variability in parameters important to snow NO₃⁻ photolysis in order to
181 investigate the potential spatial variability in snow-sourced NO_x fluxes and associated
182 reactive nitrogen recycling and redistribution across Antarctica, where observations of
183 these parameters over large spatial scales are difficult to obtain. The potential impacts of
184 nitrogen recycling between the air and snow on boundary layer chemistry as well as the

185 impacts of photolysis-driven loss of NO_3^- from the snow on the preservation of ice-core
186 NO_3^- across Antarctica are examined in this study. A major advantage of using a global
187 chemical transport model framework is the ability to examine the redistribution and loss
188 of reactive nitrogen across large spatial scales due to photolysis-driven loss of snow NO_3^- .
189 Section 2 describes the inclusion of a snowpack actinic flux parameterization and NO_3^-
190 photolysis into a global chemical transport model, GEOS-Chem. Section 3 explores the
191 implications of photolysis-driven reactive nitrogen recycling and redistribution for
192 boundary layer chemistry and the alteration of NO_3^- concentration and its isotopes
193 ultimately archived in ice cores. We end by using our model sensitivity studies to
194 highlight the largest uncertainties in our ability to model these processes as a guide for
195 future laboratory and field studies.
196

197 2. Methods

199 2.1. Incorporating Snow NO_3^- Photolysis into a Global Chemical Transport Model

200 Table 1 provides a glossary of the variables used throughout this paper.

202 2.1.1. Global Chemical Transport Model Description

203 GEOS-Chem is a global 3-dimensional (3-D) model of coupled aerosol-oxidant
204 chemistry with detailed $\text{HO}_x\text{-NO}_x\text{-VOC}\text{-O}_3\text{-BrO}_x$ tropospheric chemistry originally
205 described in Bey et al. [2001]. The model uses assimilated meteorological data from the
206 NASA Goddard Earth Observing System (GEOS-5) including winds, convective mass
207 fluxes, boundary layer depths, temperature, precipitation, and surface properties.
208 Meteorological data have 6-hour temporal resolution (3-hour for surface variables and
209 mixing depths). The TPCORE advection algorithm [*Lin and Rood, 1996*] is the transport
210 routine in GEOS-Chem and is based on the calculation of the slopes between neighboring
211 grid boxes. At the poles, neighboring grid boxes are used to estimate transport of
212 chemical species into and out of the circular polar grid box. The spectral direct and
213 diffuse downwelling surface irradiance and photolysis frequencies are calculated using
214 the Fast-JX radiative transfer module [*Wild et al., 2000, Bian and Prather, 2002, Mao et*
215 *al., 2010*]. In GEOS-Chem, aerosols can be wet deposited via scavenging in convective
216 updrafts and by rainout from convective anvils and large-scale precipitation [*Liu et al.,*
217 *2001*]. The wet deposition scheme for gases is described by Amos et al. [2012] and the
218 scavenging of aerosol by snow and cold/mixed precipitation is described by Wang et al.
219 [2011]. Dry-deposition velocities for coarse mode aerosols (radii between 1-10 mm) are
220 calculated based on aerosol size and hydroscopic growth as described in Zhang et al.
221 [2001]. Aerosol deposition to snow and ice surfaces is described by Fisher et al. [2011].
222 For smaller aerosols (radii less than 1 μm), dry deposition velocities are calculated with a
223 standard resistance-in-series scheme [*Wang et al., 1998, Wesely, 1989*].
224

225 Anthropogenic NO_x emissions are from the EDGAR 3.2-FT2000 global inventory for the
226 year 2000 [*Oliver et al., 2005*], scaled by country on the basis of energy statistics as
227 described by van Donkelaar et al. [2008]. The monthly inventory of emissions from
228 biomass burning are from the Global Fire Emissions Database (GFED2) [*van der Werf et*
229 *al., 2009*]. Soil NO_x emissions are computed using a parameterization described in
230 Hudman et al. [2012], which is a function of vegetation type, temperature, soil moisture,

231 precipitation, and fertilizer emissions. Emissions of NO_x from lightning are linked to
232 deep convection following the parameterization of *Price and Rind* [1992] and are scaled
233 globally as described by Murray et al. [2012] to match OTD/LIS climatological
234 observations of lightning flashes. The stratospheric source of NO_y (=NO_x+HNO₃) utilizes
235 monthly climatological 3-D production and loss rates from the Global Modeling Initiative
236 (GMI) model [*Allen et al.*, 2010], which captures the formation of the polar vortex and
237 PSC sedimentation [Murray et al., 2012].

238 For this work, GEOS-Chem version v9-01-01 was run at 2°x2.5° horizontal resolution
239 with 72 hybrid vertical levels using GEOS-5 meteorology from May 2009 to May 2010.
240 The model was spun up for six months prior to May 2009. There are no sub-surface
241 (snow) layers in GEOS-Chem and the three lowest vertical levels are each roughly 100
242 meters in height above Antarctica. The boundary layer in GEOS-Chem is calculated
243 using a parameterization involving the bulk Richardson number with surface friction, a
244 turbulent velocity scale, and non-local fluxes of heat and moisture [*Holtslag and Boville*,
245 1993] as implemented by Lin and McElroy [2010]. The mixing of emissions, dry
246 deposition, and concentrations of individual species within the boundary layer are
247 determined by static instability. In a stable boundary layer, the local scheme based on
248 eddy diffusivity-theory is used, and the mixing is weak. In an unstable boundary layer,
249 boundary layer mixing is triggered by large eddies. Average boundary layer mixing ratios
250 (ppbv) of species reported in this study (e.g., NO₃⁻, NO_x, OH, O₃) are mixing ratios in the
251 lowest vertical grid box (total height ~ 100 m).

252
253 Figure 1 illustrates the nitrogen recycling associated with snow NO₃⁻ photolysis as
254 included in the model. The total flux of snow-sourced NO_x from the snow, F_{NO_x} (molec
255 cm⁻² s⁻¹), is calculated using the wavelength-dependent absorption cross-section for NO₃⁻
256 photolysis ($\sigma_{NO_3^-}$, cm² molec⁻¹), the temperature (T)- and pH-dependent quantum yield for
257 NO₃⁻ photolysis (ϕ , molec photon⁻¹), the depth- and wavelength-dependent actinic flux in
258 the snow photic zone (I , photons cm⁻² s⁻¹ nm⁻¹), and the average NO₃⁻ concentration
259 ($[NO_3^-]$, molec cm⁻³) over the depth of integration. F_{NO_x} is calculated in E7 and converted
260 into units of ng N m⁻² yr⁻¹ in E8 and E9.

261
262

$$F_{NO_x} = \int_{\lambda_0}^{\lambda_1} \int_{z_0}^{z_{3e}} \sigma_{NO_3^-}(\lambda) \cdot \phi(T, pH) \cdot I(\lambda, z) \cdot [NO_3^-](z) d\lambda dz, \quad E7$$

263
264 In E7, $\sigma_{NO_3^-}$ is from Burley and Johnston [1992]. The quantum yield from Chu and
265 Anastasio [2003] assuming T=244K and pH=5 is used for the base case scenario and ϕ
266 from Zhu et al. [2010] is used for sensitivity studies. The actinic flux (I) is integrated
267 from the snow surface (z_0) to the depth of the photic zone (z_{3e}). The snow photic zone is
268 defined as three times the e-folding depth of ultraviolet (UV) actinic flux in snow (z_{3e}),
269 where 1 e-folding depth is z_e . Below z_{3e} , more than 95% of the radiation has been
270 attenuated and minimal photochemistry occurs. The flux of snow-sourced NO_x is
271 integrated over several ultraviolet wavelength bands (298-307 nm, 307-312 nm, 312-320
272 nm, 320-345 nm), which are then summed to calculate total F_{NO_x} from the photolysis of
273 snow NO₃⁻ between $\lambda=298-345$ nm. We assume that all NO_x formed in E7 is immediately
274 desorbed into the gas-phase and transported from the LLR to the interstitial air and then
275 into the overlying boundary layer [Zatko et al., 2013].

277

278 2.1.2 Calculating Radiative Transfer in Snow

279 A 2-stream, plane parallel snowpack actinic flux parameterization based on a 4-stream
 280 radiative transfer model [Grenfell, 1991] was developed and described in detail in Zatko
 281 et al. [2013] and has been implemented into GEOS-Chem for the purposes of this study.
 282 The parameterization is simple, broadly applicable, and allows for variation in snow and
 283 sky properties (e.g., solar zenith angle, cloud fraction) over time. Ice grains are assumed
 284 to be spherical in shape and light-absorbing impurities (LAI), including black carbon,
 285 brown carbon, dust, and organics, are assumed to be homogeneously distributed
 286 throughout the snow and always external to the ice grain. The snowpack actinic flux
 287 parameterization is used to calculate the UV actinic flux ($\text{photons cm}^{-2} \text{ s}^{-1} \text{ nm}^{-1}$) and the
 288 mean austral summer (DJF) e-folding depths (cm) across Antarctica (Figure 3a), which
 289 are both needed to calculate F_{NOx} . The snowpack actinic flux parameterization is most
 290 sensitive to radiation equivalent mean ice grain radii (r_e) and insoluble LAI in snow
 291 [Zatko et al., 2013]; higher concentrations of LAI in the snow and smaller r_e lead to
 292 shallower e-folding depths (z_e). Field and satellite measurements suggest significant
 293 increases in surface r_e throughout austral summer in Antarctica [Jin et al., 2008, Klein,
 294 2014]. The r_e and snow density values used in this study are from observations reported
 295 in Gallet et al. [2011] and Klein [2014] and range from 86-360 μm and 260-360 kg m^{-3} ,
 296 respectively. The mean Dome C vertical r_e profile from Gallet et al. [2011] is applied
 297 across Antarctica for all seasons except austral summer. During austral summer, larger
 298 surface r_e values are incorporated across all of Antarctica to simulate the rapid surface r_e
 299 growth reported in Klein [2014].

300

301 The concentration of black carbon (BC) in the model (Figure 3b) is calculated by scaling
 302 observed BC concentrations (C_{BC}) at Vostok [Grenfell et al., 1994] by the modeled
 303 annual average snow accumulation rates ($\text{kg m}^{-2} \text{ yr}^{-1}$) from GEOS-Chem. However, high
 304 accumulation rates in coastal regions ($700 \text{ kg m}^{-2} \text{ yr}^{-1}$) lead to unrealistically low C_{BC} .
 305 The minimum C_{BC} values used in the model are 0.08 ng g^{-1} , which is comparable to the
 306 C_{BC} values measured in high snow accumulation rate regions in Antarctica, such as in the
 307 East Antarctic sea ice zone (0.1 ng g^{-1}) [Bisiaux et al., 2012, Zatko and Warren, 2015].
 308 Insoluble non-black carbon species (nonBC) including dust, brown carbon, and organics,
 309 are responsible for the majority (up to 89% at $\lambda=305 \text{ nm}$) of the absorption of radiation at
 310 UV wavelengths [Zatko et al., 2013] in snow. These nonBC species and their
 311 concentrations have not been well quantified in snow. Based on observations reported in
 312 Zatko et al. [2013], we scale UV-absorption by insoluble nonBC to the absorption by
 313 insoluble black carbon in snow by assuming that at $\lambda=650-700 \text{ nm}$, which is a wavelength
 314 range where black carbon dominates absorption, insoluble black carbon is responsible for
 315 70% of the particulate absorption. We also assume that nonBC material has an absorption
 316 Ångstrom exponent of 5 [Doherty et al., 2010].

317

318 We neglect the influence of soluble light absorbers in the snow and only consider the
 319 influence of insoluble LAI on calculations of actinic flux profiles in snow. To determine
 320 whether soluble LAI contribute significantly to light-absorption in the snow, we calculate
 321 the total extinction coefficient for insoluble BC, insoluble nonBC, and soluble LAI
 322 following section 2.1 of Zatko et al. [2013] and using the absorption coefficients for

soluble material in snow reported in Beine et al., [2011] in northern Alaska. To our knowledge, observations of soluble light-absorbing impurities in Antarctic snow are unavailable. We use soluble LAI observations from the Arctic to provide a general estimate of the importance of soluble LAI in polar snow. The absorption coefficients (0.028 m^{-1} at $\lambda=307 \text{ nm}$) from Beine et al. [2011] are identical to the extinction coefficients because it is assumed that there is no scattering by soluble species. Insoluble C_{BC} (9 ng g^{-1}) from Barrow, Alaska [Doherty et al., 2010] were used to calculate extinction coefficients for BC and nonBC material and therefore the amount of nonBC absorption in the UV and near-visible wavelengths following Zatko et al. [2013]. Insoluble nonBC material is responsible for 9-14 times more absorption than soluble material in the wavelength range $\lambda=298\text{-}345 \text{ nm}$. Insoluble BC material is responsible for 1.5-10 times more absorption than soluble material in the wavelength range $\lambda=298\text{-}345 \text{ nm}$. The extinction coefficient is not influenced by the addition of a soluble absorber because scattering by snow grains dominates the extinction in snow. The effective co-albedo of single scattering is increased by 6-15% when soluble absorbers are included. The resulting change in z_e is at most 0.5 cm, which represents an increase of 4-9% in the wavelength region of $\lambda=298\text{-}345 \text{ nm}$.

2.1.3. Calculating NO_3^- Concentrations in Snow

The median value of sub-surface (varied depth resolution) snow NO_3^- concentrations from the ITASE campaign (60 ng g^{-1}) [Bertler et al., 2005] is used for modeled sub-surface (from 2-cm depth to the depth of the snow photic zone, z_{3e}) snow NO_3^- concentrations ($[\text{NO}_3^-]_{bot}$) across all of Antarctica. Although there is a large variation in snow NO_3^- concentrations from observations collected during the ITASE campaign (Figure 3d), there is no clear spatial pattern. Since NO_3^- concentrations in the top 2 cm of snow are up to 10 times higher than NO_3^- concentrations below 2-cm depth, the NO_3^- concentrations in the top 2 cm of snow ($[\text{NO}_3^-]_{top}$) are calculated by enhancing $[\text{NO}_3^-]_{bot}$ by a factor of 6, the median of observed NO_3^- enhancement factors (EF) in the top 2 cm of snowpack [Dibb et al., 2004, Erbland et al., 2013, Frey et al., 2009, Mayewski and Legrand, 1990, Rothlisberger et al., 2000]. Since NO_3^- concentrations are enhanced by a factor of 6 in the top 2 cm of snow, an equal amount of NO_3^- has been removed from the remainder of the photic-zone depth to maintain mass balance of nitrate within the snow column.

As mentioned in the introduction, the measured quantum yields for the dominant NO_3^- photolysis pathway (E1) range from $0.003 \text{ molec photon}^{-1}$ [Chu and Anastasio, 2003] to $0.6 \text{ molec photon}^{-1}$ [Zhu et al., 2010] at $T=253\text{K}$. A higher fraction of NO_3^- was likely present on ice surfaces in the Zhu et al. [2010] study compared to the Chu and Anastasio [2003] study due to the different sample preparation methods, and likely explains the 3 order-of-magnitude difference in quantum yields. This interpretation suggests NO_3^- on the surface of ice grains is much more photolabile compared to NO_3^- embedded within ice grains, consistent with results from Meusinger et al. [2014]. In this study, we assume that NO_3^- that is wet deposited to the snow surface is more likely to be embedded in the interior of a snow grain compared to NO_3^- that is dry deposited to the surface of the snow grain, which is a simplistic scheme designed to take nitrate recombination chemistry into account. To simulate this effect in an idealized snowpack, we scale snow NO_3^- concentrations by the fraction of dry deposition relative to total (wet + dry) deposition to

369 the Antarctic snow surface, assuming that only the fraction of dry deposited NO_3^- is
370 photolabile (F_p). The degree of migration of NO_3^- within a snow grain after deposition due
371 to snow metamorphism is unknown, which may influence the photolability of NO_3^-
372 [Domine and Shepson, 2002]. Snow NO_3^- concentrations scaled by F_p are shown in
373 Figure 3d.

374 Other modeling studies have attempted to calculate the fraction of photolabile NO_3^- in
375 snow by estimating the concentration of NO_3^- contained within the liquid-like region
376 (LLR) on the surface of ice grains (e.g., Thomas *et al.*, 2012). In this work, we do not
377 explicitly calculate NO_3^- photolysis within the LLR because there are still many
378 unknowns about the LLR [Domine *et al.*, 2013], including the distribution of NO_3^-
379 between the bulk snow and the LLR. This distribution is better understood for some
380 species, such as chloride [Cho *et al.*, 2002], but it is unclear if NO_3^- behaves similarly. In
381 this study, we have assumed that all NO_x formed in the LLR is transferred to the
382 boundary layer, which may lead to overestimates in the modeled F_{NO_x} values presented in
383 this study. The quantum yield for NO_3^- photolysis is dependent on the location of NO_3^- in
384 snow, and although there are uncertainties surrounding the location of NO_3^- in snow, in
385 this study we use the full range of measured quantum yields to provide bounds for the
386 amount of NO_x produced from snow NO_3^- photolysis.

387

388 **2.2. Model Sensitivity Studies**

389 Due to uncertainties in our understanding of snow photochemistry [Domine *et al.*, 2013],
390 we perform a variety of model sensitivity studies, as shown in Table 3. The quantum
391 yield is varied from 0.002 molec photon⁻¹ (corresponding to T=244 K) [Chu and
392 Anastasio, 2003] to 0.6 molec photon⁻¹ [Zhu *et al.*, 2010]. Snow NO_3^- concentrations
393 below 2 cm ($[\text{NO}_3^-]_{\text{bot}}$) are halved and doubled with respect to the base case scenario and
394 the impact of scaling NO_3^- concentrations by the fraction of photolabile NO_3^- (F_p) is
395 investigated. The NO_3^- enhancement factor in the top 2 cm of snowpack is varied from 1
396 to 10, based upon a range of reported observations [Dibb *et al.*, 2004, Frey *et al.*, 2009,
397 Mayewski and Legrand, 1990, Rothlisberger *et al.*, 2000]. C_{BC} is halved and doubled
398 with respect to the base case scenario. The r_e profiles are varied in three sensitivity
399 studies to examine the influence of r_e on the model-calculated mean austral summer
400 (DJF) flux of snow-sourced NO_x ($\overline{F_{\text{NO}_x}}$). The bulk extinction coefficient for snow
401 ($K_{ext,tot}$) is increased and decreased by 20% with respect to the base case scenario because
402 Libois *et al.* [2013] suggest that the spherical snow grain assumption overestimates e-
403 folding depths by a factor of 1.2. These sensitivity studies are used to provide estimates
404 of the influence of these parameters on $\overline{F_{\text{NO}_x}}$ throughout the Antarctic continent.

405

406 **2.3. Estimating the Impact of Snow NO_3^- Photolysis on Boundary Layer Chemistry 407 and Ice-Core NO_3^- Records**

408 Nitrate photolysis, followed by oxidation, recycling, and redistribution of snow-sourced
409 NO_x , influences both boundary layer chemistry and the concentration and isotopic
410 signature of NO_3^- that is ultimately preserved in ice-core records. The preservation of
411 NO_3^- in ice cores is most dependent on the amount of NO_3^- lost from the snow through
412 photolysis via transport of snow-sourced NO_x away from the site of primary deposition.

414 The methods used to explore and quantify nitrogen recycling and photolysis-driven loss
415 of NO_3^- in snow are described in the following sections.

416

417 2.3.1. Reactive Nitrogen Recycling Between the Air and Snow

418 The Nitrogen Recycling Factor (NRF) is a metric originally proposed by Davis et al.
419 [2008] to quantify the degree of reactive nitrogen recycling in snow over 1 year. The
420 NRF is calculated in E8:

421

$$422 \quad NRF = \frac{F_{\text{NO}_x}}{F_{\text{PRI}}}, \quad \text{E8}$$

423

424 In E8, F_{NO_x} ($\text{ng N m}^{-2} \text{ yr}^{-1}$) is the annual sum of NO_x released from the snow and F_{PRI} ($\text{ng N m}^{-2} \text{ yr}^{-1}$) is the annual sum of primary NO_3^- deposited to the snow. Davis et al. [2008]
425 use the NRF to describe nitrogen recycling on both macro-scale (e.g., across the East
426 Antarctic plateau) and micro-scale (e.g., the number of times one molecule of NO_3^- is
427 recycled) levels. An NRF greater than 1 suggests that multiple nitrogen recycling events
428 occur in the snow. NRF represents the average, or “bulk” degree of nitrogen recycling in
429 snow because this global modeling study cannot resolve the degree of nitrogen recycling
430 on a molecular level in the snow; some NO_3^- molecules may never be photolyzed while
431 other NO_3^- molecules may be photolyzed and recycled many times greater than NRF .
432 The NRF has implications for boundary layer chemistry because the continual re-
433 emission of NO_x enhances the effective concentration of NO_x in the boundary layer
434 [Davis et al., 2008]. Additionally, nitrogen recycling between the air and snow may alter
435 the preservation of NO_3^- in ice-core records.

436

437 2.3.2. Export of Snow-sourced Nitrate Away from the Original Site of Photolysis

438 Once snow-sourced NO_x is emitted to the atmosphere, it is subject to transport away from
439 the original site of photolysis. If snow-sourced NO_x is oxidized to HNO_3 and re-deposited
440 back to the snow surface, then there is no net photolysis-driven loss of NO_3^- from the
441 snow. However, if some of the snow-sourced NO_x is transported away from the site of
442 primary deposition, there is a net photolysis-driven loss of NO_3^- from the snow. The
443 fraction of total NO_3^- (photolabile + non-photolabile) lost from the snow driven by
444 photolysis (f) is calculated in E9:

445

$$446 \quad f = \left(\left(\frac{F_R}{F_{\text{NO}_x}} \right)^{\tau_z} - 1 \right) \cdot F_p \quad \text{E9}$$

447

448 In E9, negative values of f represent loss of NO_3^- from the snow and positive values of f
449 represent gain of NO_3^- to the snow. In E9, F_R ($\text{ng N m}^{-2} \text{ yr}^{-1}$) is the total annual flux of
450 recycled NO_3^- to the snow surface and F_{NO_x} ($\text{ng N m}^{-2} \text{ yr}^{-1}$) is the total annual flux of NO_x
451 released from the snow. F_R is calculated by subtracting the depositional flux of NO_3^- from
452 a model run without snow photochemistry from the depositional flux of NO_3^- from a
453 model run with snow photochemistry. The ratio of F_R to F_{NO_x} represents the fraction of
454 photolabile NO_3^- remaining in the snow after 1 year. As long as NO_3^- remains in the
455 photic zone, NO_3^- can continually be lost from the snow by photolysis-driven processes.
456 The preservation of NO_3^- in ice cores is dependent on the fraction of NO_3^- lost from the
457 snow through photolysis during the entire time that NO_3^- remains in the photic zone.
458

459 Provided that there are no major changes in parameters that influence snow
460 photochemistry (e.g., LAI, overhead ozone abundance) from year to year, the fraction of
461 photolabile NO_3^- lost from the snow over 1 year will be stable from year to year.

462
463 τ_z (E10) represents the number of years that NO_3^- remains in the photic zone (τ_z , years)
464 and in E9, τ_z accounts for the loss of NO_3^- that occurs during the entire time that it
465 remains in the photic zone. When NO_3^- remains in the photic zone for less than a year (τ_z
466 < 1), τ_z in E9 is set equal to 1. τ_z is calculated according to E10, where both the depth of
467 the photic zone (cm) and the total annual snow accumulation (α_r) (cm yr⁻¹) are
468 considered.

469

$$470 \quad \tau_z = \frac{z_e}{\alpha_r}, \quad \text{E10}$$

471
472 In E10, z_e (cm) is 1 e-folding depth of UV actinic flux and is used instead of z_{3e} because
473 87-91% of snow-sourced NO_x is produced within the top 1 e-folding depth. To convert
474 total annual snow accumulation rate from kg m⁻² yr⁻¹ to cm, a typical snow density for
475 Antarctica (0.36 g cm⁻³) [Grenfell *et al.*, 1994] is assumed. τ_z is the minimum number of
476 years on average that NO_3^- remains in the top one-third of the snow photic zone before
477 burial beneath because nitrogen recycling, which effectively redistributes NO_3^- upwards
478 in the snow, is not factored into E10. τ_z thus represents the lifetime of NO_3^- in snow in an
479 average sense and does not resolve photolysis and recycling of individual NO_3^-
480 molecules.

481
482 In E9, $\left(\left(\frac{F_R}{F_{\text{NO}_x}} \right)^{\tau_z} - 1 \right)$ represents the fraction of photolabile NO_3^- lost from the snow
483 through photolysis. This fraction is multiplied by F_p to calculate the fraction of total
484 (photolabile + non-photolabile) NO_3^- lost from the snow through photolysis (f). If f is 0,
485 then all snow-sourced NO_x is redeposited to the snow and there is no net loss of NO_3^- . f is
486 also 0 if the net export of snow-sourced NO_x away from the site of original photolysis is
487 balanced by net import of snow-sourced NO_x from other Antarctic locations. If f is
488 between -1 and 0, the export of local snow-sourced NO_x is higher than the deposition of
489 snow-sourced NO_x from elsewhere in Antarctica, resulting in net photolysis-driven loss
490 of NO_3^- from the snow. If f is greater than 0, the export of local snow-sourced NO_x is
491 lower than the deposition of snow-sourced NO_x from elsewhere in Antarctica, resulting in
492 net photolysis-driven gain of NO_3^- to the snow.

493
494 f is used to calculate the enrichment in ice-core $\delta^{15}\text{N}(\text{NO}_3^-)$ due solely to the impact of
495 photolysis-driven loss of NO_3^- in snow. We use a Rayleigh fractionation equation used to
496 calculate $\delta^{15}\text{N}(\text{NO}_3^-)$ [Blunier *et al.*, 2005]:

497
498
$$\delta^{15}\text{N}(\text{NO}_3^-) = \delta^{15}\text{N}(\text{NO}_3^-)_{\text{air}} \cdot (1 + f)^\epsilon - 1 \quad \text{E11}$$

499
500 In E11, $\delta^{15}\text{N}(\text{NO}_3^-)_{\text{air}}$ is the annual-averaged $\delta^{15}\text{N}$ value of boundary layer NO_3^- and ϵ
501 is the fractionation constant (-47.9‰ [Berhanu *et al.*, 2014]). In this work, we set
502 $\delta^{15}\text{N}(\text{NO}_3^-)_{\text{air}}$ equal to 0‰ to investigate the enrichment in $\delta^{15}\text{N}(\text{NO}_3^-)$ only from
503 photolysis-driven loss of NO_3^- from snow.

504

505

3. Results and Discussion

506

3.1. Parameters that Influence F_{NOX} and its Spatial Redistribution

507 Figure 2a shows modeled total annual snow accumulation rates from GEOS-Chem ($\text{kg m}^{-2} \text{ yr}^{-1}$) along with estimated total annual snow accumulation rates ($\text{kg m}^{-2} \text{ yr}^{-1}$) in
 508 Antarctica [Erblund *et al.*, 2013, Fegyveresi *et al.*, 2011, Grenfell *et al.*, 1994], ranging
 509 from 10-700 $\text{kg m}^{-2} \text{ yr}^{-1}$. The rapid decrease in snow accumulation rate from the coast to
 510 the top of the East Antarctic plateau is attributed to increased distance from the ocean
 511 (moisture source) and increased elevation. Figure 2b shows modeled annual mean surface
 512 wind divergence from May 2009 to May 2010. Figure 2b and Antarctic Mesoscale
 513 Prediction System surface wind output [Figure 3 in Parish and Bromwich, 2007] indicate
 514 that the large-scale airflow pattern in Antarctica flows from the East Antarctic plateau
 515 downslope towards the coast. There are three major regions of wind convergence in
 516 Antarctica, located near the Ross, Ronne, and Amery ice shelves.
 517

518

519 Figure 3a shows the mean austral summer (DJF) e-folding depth of UV actinic flux in
 520 snow (z_e). z_e ranges from 24 to 69 cm, with the shallowest depths on the East Antarctic
 521 plateau, due to the relatively high C_{BC} values (Figure 3b). Higher C_{BC} in snow results in a
 522 shallower z_e because UV absorption in snow is enhanced as the concentration of LAI
 523 increases [Zatko *et al.*, 2013]. In this study, coastal grid boxes are a mixture of water, sea
 524 ice, and snow-covered surfaces, and since actinic flux profiles are only calculated for
 525 snow-covered surfaces, the average z_e in coastal grid boxes are artificially shallow.
 526 Observations of e-folding depths across Antarctica are limited. France *et al.* [2011] report
 527 z_e from near-station snow at Dome C ranging from 9-20 cm at 350 nm, which agree well
 528 with our modeled z_e [Zatko *et al.*, 2013]. There are no z_e observations in Antarctica from
 529 snow without station contamination, which is representative of the majority of snow in
 530 Antarctica. Zatko *et al.* [2013] calculate z_e of 38 cm ($\lambda=298\text{-}345 \text{ nm}$) for remote Dome C
 531 snow due to lower C_{BC} far away from station contamination. The z_e for remote Dome C
 532 snow in this study (48 cm) is a factor of 1.3 larger than reported in Zatko *et al.* [2013]
 533 because larger radiation equivalent ice grain radii (r_e) are used during austral summer
 534 (based on Klein [2014]), and larger r_e grains lead to deeper z_e .
 535

536

536 Figure 3b shows snow C_{BC} , ranging from 0.08 to 0.6 ng g^{-1} . Black carbon observations at
 537 WAIS-Divide [Bisiaux *et al.* 2012], Siple Dome [Chylek *et al.*, 1992], Vostok [Grenfell *et*
 538 *al.*, 1994], South Pole [Warren and Clarke, 1990], and Dome C [Warren *et al.*, 2006] are
 539 included in Figure 3b. The highest C_{BC} values in Antarctica are found on the East
 540 Antarctic plateau (0.6 ng g^{-1}) and the spatial pattern of C_{BC} is governed by the snow
 541 accumulation rate; higher snow accumulation rates dilute C_{BC} [Doherty *et al.*, 2013]. The
 542 modeled boundary layer black carbon concentrations are relatively uniform across
 543 Antarctica (0.1-0.6 pptv) because the majority of black carbon reaches Antarctica through
 544 long-range transport (with the exception of local production from Antarctic research
 545 stations).

546

547 Figure 3c shows the fraction of dry-deposited NO_3^- compared to total deposited NO_3^-
 548 across Antarctica. The ratio of dry deposition to total deposition ranges from 0 to 0.2 in
 549 coastal Antarctica and from 0.95 to 0.99 on the East Antarctic plateau. Figure 3d shows

550 the modeled annual mean sub-surface (from 2-cm depth to the bottom of the photic zone,
551 z_{3e}) snow NO_3^- concentrations ($[\text{NO}_3^-]_{\text{bot}}=60 \text{ ng g}^{-1}$) scaled by F_p compared to averaged
552 multi-year NO_3^- observations from the ITASE campaign [Bertler *et al.*, 2005] and mean
553 asymptotic (sub-photic zone) NO_3^- mixing ratios from Erbland *et al.* [2013] and Shi *et al.*
554 [2014].

555

556 3.2. Model Sensitivity Studies

557 Table 3 shows the dependence of mean austral summer (DJF) $\overline{F_{\text{NOx}}}$ on ϕ , $[\text{NO}_3^-]_{\text{bot}}$, C_{BC} ,
558 F_p , $K_{\text{ext},\text{tot}}$, r_e . The sensitivity study results are compared to $\overline{F_{\text{NOx}}}$ from the base case
559 scenario, which is also described in Table 3. $\overline{F_{\text{NOx}}}$ is most sensitive to ϕ , which increases
560 $\overline{F_{\text{NOx}}}$ by up to a factor of 330 compared to the base case scenario. The second most
561 influential parameter is the concentration of photolabile NO_3^- ($[\text{NO}_3^-]_{\text{bot}}$ and F_p).
562 Assuming that all NO_3^- is photolabile ($F_p=1$) increases $\overline{F_{\text{NOx}}}$ by up to a factor of 7.4 (at
563 the coasts) with respect to the base case scenario. Variations in r_e , $K_{\text{ext},\text{tot}}$, EF , and C_{BC}
564 influence $\overline{F_{\text{NOx}}}$ by up to a factor of 1.3 compared to the base case scenario. Appendix A
565 shows model-calculated mean austral summer (DJF) $\overline{F_{\text{NOx}}}$ throughout Antarctica for the
566 sensitivity studies described in Table 3. The quantum yield for NO_3^- photolysis and the
567 concentration of photolabile NO_3^- are likely related to one another. This highlights the
568 need for field, laboratory, and modeling studies to investigate factors influencing these
569 parameters, such as the location of NO_3^- in ice grains.

570

571 Figure 4 shows model-calculated mean austral summer (DJF) $\overline{F_{\text{NOx}}}$ for several sensitivity
572 studies compared to previously reported F_{NOx} at Neumayer [Jones *et al.*, 2001], Halley
573 [Bauguitte *et al.*, 2012, Jones *et al.*, 2011], South Pole [Oncley *et al.*, 2004, Wang *et al.*,
574 2008, Zatko *et al.*, 2013], Dome C [Frey *et al.*, 2013, Zatko *et al.*, 2013], and WAIS-
575 Divide [Mascllin *et al.*, 2013]. The flux of snow-sourced NO_x is overestimated by three
576 orders of magnitude compared to observations when ϕ from Zhu *et al.* [2010] is used to
577 calculate $\overline{F_{\text{NOx}}}$. In contrast, model-calculated $\overline{F_{\text{NOx}}}$ using ϕ from Chu and Anastasio
578 [2003] provides better agreement with the observations, but is lower than the
579 observations by 14-78%. Use of the fraction of dry-deposited NO_3^- (F_p) to scale the
580 concentration of photolabile NO_3^- lowers $\overline{F_{\text{NOx}}}$ by up to 85% along the coast, but has
581 little impact on the East Antarctic plateau due to the high fraction of dry deposited NO_3^-
582 (Figure 3c). The spatial patterns of $\overline{F_{\text{NOx}}}$ in Figure 4 are largely governed by the depth of
583 the photic zone (z_e) across Antarctica (Figure 3a), which are inversely related to LAI
584 concentrations. The spatial patterns of $\overline{F_{\text{NOx}}}$ are also influenced by the fraction of
585 photolabile NO_3^- , which is lowest at the coast in the model.

586

587 Previously reported F_{NOx} values are calculated from measurements of NO_x concentration
588 gradients and turbulent diffusivity [Jones *et al.*, 2001, 2011, Frey *et al.*, 2013] or
589 calculated based on observed NO gradients and assuming photochemical steady-state
590 [Oncley *et al.*, 2004], by incorporating observations into 1-D multi-phase chemistry
591 models [Bauguitte *et al.*, 2012, Boxe and Saiz-Lopez., 2008, Wang *et al.*, 2008], or by
592 using depth-integrated F_{NOx} calculations similar to E7 [France *et al.*, 2011, Mascllin *et al.*,
593 2013, Zatko *et al.*, 2013]. Observations of F_{NOx} represent either noontime maxima
594 [Bauguitte *et al.*, 2012, Frey *et al.*, 2013, Jones *et al.*, 2001, Zatko *et al.*, 2013], daily
595 averages [Jones *et al.*, 2011, Mascllin *et al.*, 2013], or averages over the duration of the

596 field campaign [*Oncley et al.*, 2004, *Wang et al.*, 2008] (see Table 4 in *Masclin et al.*,
597 [2013]). There is a wide range of reported $\overline{F_{NOx}}$ at many of these locations; $2.4\text{-}17 \times 10^8$
598 molec $\text{cm}^{-2} \text{s}^{-1}$ at Dome C [*France et al.*, 2011, *Frey et al.*, 2013, *Zatko et al.*, 2013], 3.2-
599 22×10^8 molec $\text{cm}^{-2} \text{s}^{-1}$ at South Pole [*Oncley et al.*, 2004, *Wang et al.*, 2008, *Zatko et al.*,
600 2013], $2.4\text{-}12.6 \times 10^8$ molec $\text{cm}^{-2} \text{s}^{-1}$ at Halley [*Bauguitte et al.*, 2012, *Jones et al.*, 2011],
601 $2.1\text{-}3.3 \times 10^8$ molec $\text{cm}^{-2} \text{s}^{-1}$ at Neumayer [*Jones et al.*, 2001], 42.5×10^8 molec $\text{cm}^{-2} \text{s}^{-1}$ at
602 WAIS-Divide [*Masclin et al.*, 2013].

603

604 Regardless of the time period that the F_{NOx} observations represent, all F_{NOx} values for
605 each location are averaged together and presented in Figure 4c and Figure 4d.
606 Unfortunately, the actinic flux parameterization used here [*Zatko et al.*, 2013] is unable to
607 resolve $\overline{F_{NOx}}$ directly at the coast because coastal grid boxes are a mixture of ocean, sea
608 ice, and land, which prevents direct comparison of $\overline{F_{NOx}}$ at Halley and Neumayer. Since
609 the flux of snow-sourced NO_x is overestimated by three orders of magnitude compared to
610 observations when the quantum yield from Zhu et al. [2010] is used, all following results
611 (Figures 5-10) are calculated using the Chu and Anastasio [2003] quantum yield
612 ($\phi=1.3 \times 10^{-3}$). Additionally, to approximate the potential spatial variability in the fraction
613 of NO₃⁻ that is photolabile, we scale snow NO₃⁻ by F_p in Figures 5-10. Figure 4d shows
614 the $\overline{F_{NOx}}$ values, ranging from $0.5\text{-}7.8 \times 10^8$ molec $\text{cm}^{-2} \text{s}^{-1}$, used in Figures 5-10. All the
615 other parameters used to calculate $\overline{F_{NOx}}$ in following sections and in Figures 5-10 are
616 described in the base-case scenario in Table 3.

617

618 3.3. Redistribution and Recycling of Reactive Nitrogen Across Antarctica

619 Figure 5a shows the total annual depositional flux of primary NO₃⁻ (F_{PRI}), which ranges
620 from $0.9\text{-}35 \times 10^5$ ng N $\text{m}^{-2} \text{yr}^{-1}$ and is highest at the coasts due to its relative proximity to
621 NO_x-source regions in lower latitudes. An adjoint modeling study by Lee et al. [2014]
622 suggests that boundary layer NO₃⁻ abundance in Antarctica is dominated by NO₃⁻
623 transport to Antarctica originating from NO_x emissions from 25-65°S during austral
624 winter and by thermal decomposition of peroxyacetyl nitrate (PAN) as it descends from the
625 free troposphere in all other seasons. Figure 5b shows the total annual depositional flux
626 of recycled NO₃⁻ (F_R), which ranges from $0.7\text{-}31 \times 10^5$ ng N $\text{m}^{-2} \text{yr}^{-1}$ and is also highest at
627 the coasts due to transport from the Antarctic interior by katabatic winds. F_{PRI} and F_R are
628 comparable in magnitude to the total annual flux of snow-sourced NO_x to the atmosphere
629 (F_{NOx}), which ranges from $2\text{-}23 \times 10^5$ ng N $\text{m}^{-2} \text{yr}^{-1}$ (Figure 4d). Figure 5c shows that
630 recycled nitrogen (F_R) is the dominant form of NO₃⁻ deposition across Antarctica, except
631 along the coastline where it represents as little as 11% of the deposition flux, and is most
632 important in regions of wind convergence such as the Ronne, Ross, and Amery ice
633 shelves.

634

635 To further investigate the role that wind patterns have on the redistribution of NO₃⁻ across
636 Antarctica, we alternately turn off the upward F_{NOx} in East Antarctica and in West
637 Antarctica to examine the influence of each region on NO₃⁻ redistribution across
638 Antarctica. Figure 6 compares F_R in these sensitivity studies to F_R in the base case
639 scenario. The large reduction in F_R when F_{NOx} is separately turned off in East and West
640 Antarctica demonstrates that little snow-sourced NO₃⁻ is transported between East and West
641 Antarctica, likely due to the influence of the trans-Antarctic mountains on

642 atmospheric transport. However, recycled NO_3^- is present in West Antarctica where F_{NO_x}
643 has been turned off, suggesting that some snow-sourced NO_3^- from East Antarctica is
644 transported across the trans-Antarctic mountains likely due to the influence of katabatic
645 winds originating from the East Antarctic plateau.

646
647 Figure 7 shows the Nitrogen Recycling Factor (NRF). Across Antarctica, NRF ranges
648 from 0 to 16, indicating that nitrogen is recycled multiple times over the course of 1 year
649 across most of Antarctica, with the exception of the coasts. The spatial pattern of NRF is
650 governed by the flux of snow-sourced NO_x to the atmosphere ($\overline{F_{\text{NO}_x}}$, Figure 4d), which is
651 influenced by the depth of the photic zone (z_e) and the concentration of photolabile
652 nitrate. The spatial pattern of NRF is also dependent on F_{PRI} , which is highest at the coast
653 and lowest on the East Antarctica plateau. NRF values are lowest near the coast because
654 the fraction of photolabile NO_3^- is small and F_{PRI} values are high. The maximum NRF
655 values occur partway up the plateau, corresponding to maximum $\overline{F_{\text{NO}_x}}$ values. Erbland et
656 al. [2015] use a multi-layer snow chemistry column model along with snow and
657 atmospheric NO_3^- concentration and isotopic measurements to estimate the NRF at Dome
658 C. The difference in model-estimates of nitrogen recycling at Dome C in Erbland et al.
659 [2015] (4 recycling events) and in this study (9 recycling events) is at least partially due
660 to the assumption in Erbland et al. that 20% of snow-sourced NO_3^- is transported away
661 from Dome C via katabatic winds. We use our global chemical transport modeling
662 framework to calculate that 25% of snow-sourced NO_3^- is transported away at Dome C,
663 which is slightly larger than the assumption in Erbland et al. [2015]. Larger NO_3^- export
664 fractions will lead to larger loss of snow nitrate, which may also lead to a larger number
665 of recycling events via transport and redeposition of snow-sourced NO_x throughout East
666 Antarctica. Davis et al. [2008] use estimates of atmospheric NO_x overhead-column
667 burdens and average NO_x atmospheric lifetimes along with primary nitrogen deposition
668 measurements from Legrand and Kirchner [1990] to estimate the NRF in East Antarctica.
669 Davis et al. [2008] estimate an NRF of 1.8, which is roughly 3 to 6 times lower than the
670 modeled East Antarctic NRF values in this study ($NRF=5-10$), although Davis et al. state
671 that their estimated NRF value could be factors of 3 to 5 times higher due to uncertainties
672 in primary nitrogen deposition estimates.

673
674 **3.4. Impact of Reactive Nitrogen Recycling on Boundary Layer Chemistry**
675 The height of the boundary layer will strongly influence the abundance of NO_3^- , reactive
676 nitrogen oxides, and oxidants emitted or formed at or near the surface. At many Antarctic
677 stations (e.g., Neumayer, South Pole, Dome C, Halley, Kohnen) there is a wide range of
678 observed boundary layer heights during austral summer (10-600 m [Casasanta et al.,
679 2014, Davis et al., 2004, Handorf, 1996, Jones et al., 2006, 2008, King et al., 2006,
680 Kodama et al., 1985, Konig-Langlo et al., 1998, Neff et al., 2008, Oncley et al., 2004,
681 Travouillon et al., 2008, Weller et al., 1999]), and although modeled boundary layer
682 heights are not systematically biased in one direction compared to observations, they
683 often do not agree well. Therefore, only the relative impacts of snow photochemistry on
684 reactive nitrogen and oxidant abundances are compared in this study. The impact of snow
685 photochemistry on boundary layer chemistry can be examined by considering factor
686 changes in boundary layer NO_x , NO_3^- , OH , and O_3 mixing ratios between simulations
687 with and without snow NO_3^- photolysis. As shown in Figure 8, the inclusion of a snow

688 NO_x source leads to factor increases in boundary layer mixing ratios of NO_x from 7.0-
689 31.6, gas-plus aerosol-phase nitrate from 3.9-38.1, OH from 3.6-6.7, and O₃ from 1.3-2.0.
690 The largest factor increases are in West Antarctica, particularly near the Ross and Ronne
691 ice shelves, where winds carrying photo-produced species converge. The surface
692 transport pattern is especially important for the redistribution of the longer-lived species
693 NO₃⁻ and O₃. Other snow photochemical reactions mentioned in the introduction but not
694 included in this modeling study will also impact oxidant abundances, but the effects of
695 each photochemical reaction are not be additive due to the highly non-linear nature of
696 oxidant cycling.

697

698 **3.5. Implications for Ice-Core Records of Nitrate Concentrations and Isotopes**

699 Figure 9a shows the minimum number of years that snow NO₃⁻ remains in the photic
700 zone on average, τ_z (E9). NO₃⁻ remains in photic zone for 3 months near the Antarctic
701 coasts and up to 7.5 years on the East Antarctic plateau before burial below the photic
702 zone. The spatial pattern of τ_z is governed by the snow accumulation rate, both directly
703 and indirectly through its influence on C_{BC} . The spatial pattern of τ_z is in agreement with
704 the expectation that NO₃⁻ remains in the photic zone the longest in areas with low snow
705 accumulation rates.

706

707 Figure 9b shows the fraction of NO₃⁻ gained or lost from the snow through photolysis (f ,
708 E11), which ranges from -0.99 to 0.21. The positive f values indicate regions with net
709 gain of NO₃⁻ to the snow resulting from the spatial redistribution of NO₃⁻ driven by snow
710 photochemistry. In regions of convergence, such as over the Ronne Ice Shelf, and parts of
711 the coast, there is a net gain of snow-sourced NO₃⁻. There is a sharp gradient in f between
712 the plateau and the coast, with the largest loss of snow NO₃⁻ on the East Antarctic
713 plateau. On the East Antarctic plateau, most photolyzed NO₃⁻ is transported away by
714 katabatic winds, but along the coast, the photolysis-driven loss of NO₃⁻ from the snow is
715 minimal due to high snow accumulation rates and transport of snow-sourced NO₃⁻ from
716 the continental interior. The spatial pattern of f is largely influenced by the number of
717 years that NO₃⁻ remains in the photolytic zone (τ_z), the concentration of photolabile NO₃⁻
718 (F_p), and wind patterns across Antarctica.

719

720 Figure 9c shows modeled enrichments in ice-core $\delta^{15}\text{N}(\text{NO}_3^-)$ from photolysis-driven loss
721 of NO₃⁻ in snow, compared to sub-photic zone $\delta^{15}\text{N}(\text{NO}_3^-)$ observations from Erbland et
722 al. [2013], Frey et al. [2009], Jarvis, [2008], Shi et al., [2014], and Sofen et al. [2014].
723 The $\delta^{15}\text{N}(\text{NO}_3^-)$ values at Dome C and along the transect from Dumont d'Urville to
724 Dome C are calculated asymptotic $\delta^{15}\text{N}(\text{NO}_3^-)$ values from Erbland et al. [2013] and Frey
725 et al. [2009], which are representative of snow depths well below the photic zone at
726 Dome C. The $\delta^{15}\text{N}(\text{NO}_3^-)$ values along the transect from Dome A towards Zhongshan are
727 asymptotic $\delta^{15}\text{N}(\text{NO}_3^-)$ values calculated in Shi et al. [2014]. The $\delta^{15}\text{N}(\text{NO}_3^-)$ values at
728 WAIS-Divide [Sofen et al., 2014] and South Pole [Jarvis, 2008] are average ice-core
729 $\delta^{15}\text{N}(\text{NO}_3^-)$ measurements from 1900-2000 CE, which are also representative of
730 $\delta^{15}\text{N}(\text{NO}_3^-)$ values well below the snow photic zone. Model-calculated ice-core
731 $\delta^{15}\text{N}(\text{NO}_3^-)$ values range from 0‰ to 363‰. The modeled enrichments in ice-core
732 $\delta^{15}\text{N}(\text{NO}_3^-)$ values are generally higher than the sub-photic zone $\delta^{15}\text{N}(\text{NO}_3^-)$ observations
733 presented in Figure 9c, however, boundary layer $\delta^{15}\text{N}(\text{NO}_3^-)$ observations are negative in

734 both coastal [Morin *et al.*, 2009, Savarino *et al.*, 2007, Wagenbach *et al.*, 1998] and
735 continental [Erbland *et al.*, 2013, Frey *et al.*, 2009] Antarctica, making modeled
736 $\delta^{15}\text{N}(\text{NO}_3^-)$ values biased high by up to ~40‰ since we assume that the $\delta^{15}\text{N}$ of
737 atmospheric nitrate (NO_3^- and HNO_3) deposited to the snow surface is always equal to
738 0‰. The modeled ice-core $\delta^{15}\text{N}(\text{NO}_3^-)$ values resulting from the photolysis-driven loss
739 of snow nitrate are sensitive to the fractionation constant (ϵ). The fractionation constant
740 is varied over the full range of values reported in Erbland et al [2013], Frey et al., [2009],
741 and Shi et al. [2014]; an ϵ of -90‰ increases modeled ice-core $\delta^{15}\text{N}(\text{NO}_3^-)$ by a factor of
742 2 and an ϵ of -10‰ decreases modeled ice-core $\delta^{15}\text{N}(\text{NO}_3^-)$ by a factor of 5 across
743 Antarctica. Both the modeled and observed $\delta^{15}\text{N}(\text{NO}_3^-)$ values show that $\delta^{15}\text{N}(\text{NO}_3^-)$ is
744 most enriched on the East Antarctic plateau, where the fraction of NO_3^- lost from the
745 snow through photolysis is highest.

746

747 3.6. Relationship Between Nitrogen Recycling and Photolytic-loss of NO_3^- in Snow

748 The degree of photolysis-driven loss of snow NO_3^- is determined by both rates of
749 photolysis and transport patterns across the Antarctic continent. The spatial patterns of
750 recycling (NRF , Figure 7) and loss (f , Figure 9b) differ across Antarctica and Figure 10
751 shows the relationship between f and NRF across Antarctica. The magnitude of nitrogen
752 recycling and degree of photolysis-driven loss of snow NO_3^- are well correlated ($r^2 > 0.8$,
753 $p < 0.001$) in regions where NO_3^- remains in the photic zone for less than 3 years ($\tau_z < 3$)
754 (Figure 10a). The relationship between recycling and loss breaks down in locations where
755 NO_3^- remains in the photic zone for more than 3 years (Figure 10b). The relationship
756 between recycling and loss weakens with increasing τ_z because recycling of reactive
757 nitrogen occurs at or near the surface only, while loss of NO_3^- occurs throughout the
758 depth of snow photic zone. The number of years that NO_3^- remains in the snow photic
759 zone (τ_z , E10) is mainly dependent on snow accumulation rates and the concentrations of
760 light-absorbing impurities in snow, which are partially governed by snow accumulation
761 rates. In the present climate, τ_z less than 3 years corresponds to snow accumulation rates
762 higher than $85 \text{ kg m}^{-2} \text{ a}^{-1}$.

763

764 4. Conclusions

765 We have incorporated the photolysis of snow NO_3^- into a global chemical transport
766 model (GEOS-Chem) for the first time in order to calculate the flux and redistribution of
767 nitrogen in Antarctic snowpack. An important goal of this study is to investigate the
768 impact of snowpack NO_3^- photolysis on boundary layer chemistry and the preservation of
769 NO_3^- concentration and isotopes in Antarctic ice cores.

770

771 The calculated flux of snow-sourced NO_x from Antarctic snow ($0.5\text{--}7.8 \times 10^8 \text{ molec cm}^{-2} \text{ s}^{-1}$)
772 is in general agreement with snow NO_x -flux observations when using a quantum yield
773 for snow NO_3^- photolysis on the order of $10^{-3} \text{ molec photon}^{-1}$ [Chu and Anastasio, 2003].
774 The flux of snow-sourced NO_x is overestimated by 2-3 orders of magnitude when the
775 quantum yield from Zhu et al. [2010] is used along with various assumptions for the
776 amount of photolabile NO_3^- . The modeled spatial pattern of the flux of snow-sourced
777 NO_x is determined by the patterns of light-absorbing impurity concentrations in snow and
778 the fraction of photolabile NO_3^- across Antarctica. In the model, the spatial pattern of
779 light-absorbing impurities is strongly influenced by snow accumulation rates and the

780 spatial pattern of photolabile NO_3^- in the model is influenced by the amount of wet
781 deposited NO_3^- compared to total deposited NO_3^- across Antarctica. Total snow NO_3^-
782 concentrations were kept spatially constant in this study; however, spatial variations in
783 snow NO_3^- concentrations would also influence the spatial pattern of F_{NO_x} across
784 Antarctica. However, observations of snow NO_3^- concentrations across Antarctica show
785 no clear spatial pattern. Snow-sourced NO_x is subject to transport across Antarctica, and
786 recycled NO_3^- makes up a large fraction of the depositional NO_3^- flux across the Antarctic
787 continent, especially in regions of convergence over the Ronne, Ross, and Amery ice
788 shelves.

789
790 The inclusion of snow-sourced NO_x in GEOS-Chem leads to factor increases in boundary
791 layer mixing ratios for NO_x ranging from 7.0-31.6, gas and aerosol phase nitrate ranging
792 from 3.9-38.1, OH ranging from 3.6-6.7, and O_3 ranging from 1.3-2.0. The incorporation
793 of additional snow photochemical reactions into GEOS-Chem will also impact oxidant
794 abundances, but the effects of each photochemical reaction are not be additive due to the
795 highly non-linear nature of oxidant cycling.

796
797 The Nitrogen Recycling Factor (*NRF*) ranges from 0.07 to 15.8, suggesting that nitrogen
798 is recycled multiple times on average over the course of one year across all of Antarctica,
799 except at the coasts where snow accumulation rates are high. Nitrate can remain in the
800 photic zone for up to 7.5 years in Antarctic snow and is recycled multiple times (up to 57,
801 on average) before burial beneath the photic zone in Antarctica. The fraction of NO_3^- lost
802 from the snow through photolysis ranges from -0.99 to 0.21, where negative values
803 indicate net loss of NO_3^- from the snow. Photolysis of snow NO_3^- results in a net gain of
804 NO_3^- in parts of West Antarctica, such as near the Ronne Ice Shelf where winds
805 converge. The fraction of NO_3^- lost from the snow through photolysis is highest on the
806 East Antarctic plateau (up to -0.99). The fraction of NO_3^- lost from the snow through
807 photolysis is used to calculate the enrichment in ice-core $\delta^{15}\text{N}(\text{NO}_3^-)$ solely from
808 photolysis-driven NO_3^- loss in snow. The modeled enrichment in ice-core $\delta^{15}\text{N}(\text{NO}_3^-)$
809 ranges from 0‰ to 363‰ and are in agreement with the broad-scale spatial patterns of
810 observed sub-photic zone $\delta^{15}\text{N}(\text{NO}_3^-)$ observations. A significant relationship exists
811 between nitrogen recycling and photolysis-driven loss of snow NO_3^- when NO_3^- remains
812 in the photic zone for less than 3 years ($\tau_z < 3$), corresponding to a snow accumulation
813 rate greater than $85 \text{ kg m}^{-2} \text{ a}^{-1}$ in the present day. Since the spatial variability of Antarctic
814 ice-core $\delta^{15}\text{N}(\text{NO}_3^-)$ is mainly determined by the fractional loss of snow NO_3^- ,
815 observations of $\delta^{15}\text{N}(\text{NO}_3^-)$ in snow and ice can be used to estimate both the degree of
816 recycling and loss of snow NO_3^- in Antarctica as long as this condition is met. The
817 relationship between recycling and loss can be useful for the interpretation of the oxygen
818 isotopic composition of ice-core NO_3^- (e.g., Sofen et al. [2014]). We note that the
819 relationship between τ_z and snow accumulation rate may vary in different climates
820 depending on the concentrations of light-absorbing impurities in snow [Geng et al.,
821 2015].

822
823 This is the first modeling study to incorporate snow NO_3^- photolysis into a global
824 chemical transport model to investigate the impacts of a snow- NO_x source on boundary
825 layer chemistry and nitrogen recycling and redistribution across Antarctica. Model results

826 shown here are broadly consistent with observations of the flux of NO_x from the
827 Antarctic snowpack and snow δ¹⁵N(NO₃⁻), suggesting that the model captures the large-
828 scale features of nitrogen recycling and loss across the Antarctic continent. Model
829 sensitivity studies suggest that the flux of snow-sourced NO_x and loss of snow NO₃⁻ is
830 most sensitive to the quantum yield for NO₃⁻ photolysis and the concentration of
831 photolabile NO₃⁻, which are likely related to one another. We suggest that future field,
832 laboratory, and modeling studies continue to focus on gaining a better understanding of
833 the quantum yield for NO₃⁻ photolysis and the concentration of photolabile NO₃⁻.
834 Updated information about the quantum yield for NO₃⁻ photolysis and the concentration
835 of photolabile NO₃⁻ in snow along with additional snow photochemical reactions can be
836 incorporated into this modeling framework in the future, which will continue to improve
837 our understanding of the impacts of snow photochemistry on boundary layer chemistry
838 and the preservation of NO₃⁻ and other photochemically-active species in ice cores.
839

840 Acknowledgments

841 We acknowledge support from NSF PLR 1244817, NSF PLR 0944537, NSF PLR
842 1446904, and an EPA STAR graduate fellowship to M.C. Zatko. The authors thank Steve
843 Warren, Sarah Doherty, Thomas Grenfell, and Quentin Libois for helpful discussions
844 about light-absorbing impurities in snow and their influence on snow photochemistry. We
845 thank Joseph Erbland for many helpful comments and discussions about nitrogen
846 recycling. Joel Thornton and Lyatt Jaeglé also provided many helpful comments about
847 this work. We also thank Paul Hezel and Yanxu Zhang for helping M.C. Zatko learn
848 GEOS-Chem. Lastly, we thank Qianjie Chen for helpful feedback on paper drafts and
849 Martin Schneebeli for providing useful advice about snow grain profiles in Antarctic
850 snow.

851 852 References

- 853 Allen, D., Pickering, K., Duncan, B., Damon, M.: Impact of lightning NO emissions on
854 North American photochemistry as determined using the Global Modeling Initiative
855 (GMI) model. *J. Geophys. Res.*, 115, D22301, doi:10.1029/2010JD014062, 2010.
- 856 Alexander, B., Savarino, J., Kreutz, K.J., Thiemens, M.H.: Impact of preindustrial
857 biomass burning emissions on the oxidation pathways of tropospheric sulphur and
858 nitrogen. *J. Geophys. Res.*, 109, D08303, doi:10.1029/2003JD004218, 2004.
- 859 Amos, H. M., Jacob, D.J., Holmes, C.D., Fisher, J.A., Wang, Q., Yantosca, R.M., Corbitt,
860 E.S., Galarneau, E., Rutter, A.P., Gustin, M.S., Steffen, A., Schauer, J.J., Graydon, J.A.,
861 St. Louis, V.L., Talbot, R.W., Edgerton, E.S., Zhang, Y., Sunderland, E.M.: Gas-Particle
862 Partitioning of Atmospheric Hg(II) and Its Effect on Global Mercury Deposition, *Atmos.*
863 *Chem. Phys.*, **12**, 591-603, 2012.
- 864 Anastasio, C., Galbavy, E. S., Hutterli, M. A., Burkhardt, J. F., Friel, D. K.:
865 Photoformation of hydroxyl radical on snow grains at Summit, Greenland. *Atmos.*
866 *Environ.*, 41, 5110-5121, doi:10.1016/j.atmosenv.2006.12.011, 2007.

- 871 Anastasio, C. and Chu, L.: Photochemistry of nitrous acid (HONO) and nitrous acidium
872 ion (H_2ONO^+) in aqueous solution and ice. *Environ. Sci. Tech.*, 43, 1108-1114, 2009.
873
- 874 Bauguitte, S.J.-B., Bloss, W.J., Evans, M.J., Salmon, R.A., Anderson, P.S., Jones, A.E.,
875 Lee, J.D., Saiz-Lopez, A., Roscoe, H.K., Wolff, E.W., Plane, J.M.C.: Summertime NOx
876 measurements during the CHABLIS campaign: can source and sink estimates unravel
877 observed diurnal cycles? *Atmos. Chem. Phys.*, 12, 989-1002, doi:10.5194/acp-12-989-
878 2012, 2012.
879
- 880 Beine, H., Anastasio, C., Esposito, G., Patten, K., Wilkening, E., Domine, F., Voisin, D.,
881 Barret, M., Houdier, S., Hall, S.: Soluble, light-absorbing species in snow at Barrow,
882 Alaska. *J. Geophys. Res.*, 116, D00R05, doi: 10.1029/2011JD016181, 2011.
883
- 884 Berhanu, T. A., Meusinger, C., Erbland, J., Jost, R., Bhattacharya, S. K., Johnson, M. S.,
885 Savarino, J.: Laboratory study of nitrate photolysis in Antarctic snow. II. Isotopic effects
886 and wavelength dependence. *J. Chem. Phys.*, 140, 244306, doi:10.1063/1.4882899, 2014.
887
- 888 Bertler, N., Mayewski, P. A., Aristarain, A., Barrett, P., Becagli, S., Bernardo, R., Bo, S.,
889 Xiao, C., Curran, M., Qin, D., Dixon, D., Ferron, F., Fischer, H., Frey, M., Frezzotti, M.,
890 Fundel, F., Genthon, C., Gragnani, R., Hamilton, G., Handley, M., Hong, S., Isaksson, E.,
891 Kang, J., Ren, J., Kamiyama, K., Kanamori, S., Karkas, E., Karlof, L., Kaspari, S.,
892 Kreutz, K., Kurbatov, A., Meyerson, E., Ming, Y., Zhang, M., Motoyama, H., Mulvaney,
893 R., Oerter, H., Osterberg, E., Proposito, M., Pyne, A., Ruth, U., Simoes, J., Smith, B.,
894 Snead, S., Teinila, K., Traufetter, F., Udisti, R., Virkkula, A., Watanabe, O., Williamson,
895 R., Winther, J-G., Li, Y., Wolff, E., Li, Z., Zielinski, A.: Snow chemistry across
896 Antarctica, *Annals of Glaciology*, 41(1), 167- 179, 2005.
897
- 898 Bey, I., Jacob, D.J., Yantosca, R.M., Logan, J.A., Field, B.D., Fiore, A.M., Li, Q., Liu,
899 H.Y., Mickley, L.J., Schultz, M.G.: Global modeling of tropospheric chemistry with
900 assimilated meteorology: Model description and evaluation, *J. Geophys. Res.*, 106(D19),
901 23073-23095, 2001.
902
- 903 Bian, H.S., Prather, M.J.: Fast-J2: Accurate simulation of stratospheric photolysis in
904 global chemical models. *J. Atmos. Chem.*, 41, 281-296, 2002.
905
- 906 Bisiaux, M. M., Edwards, R., McConnell, J. R., Curran, M. A. J., Van Ommen, T. D.,
907 Smith, A. M., Neumann, T. A., Pasteris, D. R., Penner, J. E., Taylor, K.: Changes in
908 black carbon deposition to Antarctica from two high-resolution ice core records, 1850-
909 2000 AD. *Atmos. Chem. Phys.*, 12, 4107-4115, doi: 10.5194/acp-12-4107-2012, 2012.
910
- 911 Bloss, W.J., Lee, J.D., Heard, D.E., Salmon, R.A., Bauguitte, S.J-B., Roscoe, H.K.,
912 Jones, A.E.: Observations of OH and HO₂ radicals in coastal Antarctica. *Atmos. Chem.*
913 *Phys.*, 7, 4171-4185, 2007.
914

- 915 Boxe, C.S., Colussi, A.J., Hoffmann, M.R., Murphy, J.G., Wolldridge, P.J., Bertram,
916 T.H., Cohen, R.C.: Photochemical production and release of gaseous NO₂ from nitrate-
917 doped water ice. *J. Phys. Chem.*, A, 109, 8520-8525, 2005.
918
- 919 Boxe, C.S., Saiz-Lopez, A.: Multiphase modeling of nitrate photochemistry in the quasi-
920 liquid layer (QLL): implications for NO_x release from the Arctic and coastal Antarctic
921 snowpack. *Atmos. Chem. Phys.*, 8, 4855-4864, 2008.
922
- 923 Blunier, T., Gregoire, F. L., Jacobi, H.-W., and Quansah, E.: Isotopic view on nitrate loss
924 in Antarctic surface snow. *Geophys. Res. Lett.*, 32, L13501, doi:10.1029/2005GL023011,
925 2005.
926
- 927 Casasanta, G., Pietroni, I., Petenko, I., Argentini, S.: Observed and modelled convective
928 mixing-layer height in Dome C, Antarctica. *Boundary-Layer Meteorol.*, 151, 597-608,
929 doi:10.1007/s10546-014-9907-5, 2014.
930
- 931 Chen, G., Davis, D., Crawford, J., Hutterli, L.M., Huey, L.G., Slusher, D., Mauldin, L.,
932 Eisele, F., Tanner, D., Dibb, J., Buhr, M., McConnell, J., Lefer, B., Shetter, R., Blake, D.,
933 Song, C.H., Lombardi, K., Arnoldy, J.: A reassessment of HO_x South Pole chemistry
934 based on observations recorded during ISCAT 2000. *Atmos. Environ.*, 38, 5451-5461,
935 2004.
936
- 937 Chu, L., and Anastasio. C.: Quantum Yields of Hydroxyl Radicals and Nitrogen Dioxide
938 from the Photolysis of Nitrate on Ice. *J. Phys. Chem. A.*, 107, 9594-9602, 2003.
939
- 940 Cho, H., Shepson, P.B., Barrie, L.A., Cowin, J.P., Zaveri, R.: NMR Investigation of the
941 Quasi-Brine Layer in Ice/Brine Mixtures. *J. Phys. Chem. B.*, 106, 11226-11232, 2002.
942
- 943 Chylek, P., Johnson, B., Wu, H.: Black carbon concentration in Byrd station ice core –
944 From 13,000 to 700 years before present. *Ann. Geophys.*, 10, 625-629, 1992.
945
- 946 Davis, D., Chen, G., Buhr, M., Crawford, J., Lenschow, D., Lefer, B., Shetter, R., Eisele,
947 F., Mauldin, L., Hogan, A.: South Pole NO_x Chemistry: an assessment of factors
948 controlling variability and absolute levels. *Atmos. Environ.*, 38, 5375-5388, 2004.
949
- 950 Davis, D. D., Seelig, J., Huey, G., Crawford, J., Chen, G., Wang, Y., Buhr, M., Helmig,
951 D., Neff, W., Blake, D., Arimoto, R., Eisele, F.: A reassessment of Antarctic plateau
952 reactive nitrogen based on ANTCI 2003 airborne and ground based measurements.
953 *Atmos. Environ.*, 42, 2831-2848, doi:10.1016/j.atmosenv.2007.07.039, 2008.
954
- 955 Dibb, J. E., Huey, G. L., Slusher, D. L., and Tanner, D. J.: Soluble reactive nitrogen
956 oxides at South Pole during ISCAT 2000. *Atmos. Environ.*, 38, 5399-5409, 2004.
957
- 958 Doherty, S. J., Warren, S. G., Grenfell, T. C., Clarke, A. D., and Brandt, R. E.: Light-
959 absorbing impurities in Arctic snow. *Atmos. Chem. Phys.*, 10, 11647-11680,
960 doi:10.5194/acp-10-11647-2010, 2010.

- 961
962 Doherty, S. J., Grenfell, T.C., Forsstrom, S., Hegg, D.L., Brandt, R.E., Warren, S.G.:
963 Observed vertical redistribution of black carbon and other insoluble light-absorbing
964 particles in melting snow, *J. Geophys. Res. Atmos.*, 118, 1-17, doi:10.1002/jgrd.50235,
965 2013.
966
967 Domine, F., Shepson, P. B.: Air-snow interactions and atmospheric chemistry, *Science*,
968 297, 1506–1510, 2002.
969
970 Domine, F., Bock, J., Voisin, D., Donaldson, D. J.: Can we model snow photochemistry?
971 Problems with the current approaches. *J. Phys. Chem. A*, 117, 4733-4749, doi:
972 10.1021/jp3123314 2013.
973
974 Erbland, J., Vicars, W.C., Savarino, J., Morin, S., Frey, M.M., Frosini, D., Vince, E.,
975 Martins, J.M.F.: Air-snow transfer of nitrate on the East Antarctic Plateau – Part 1:
976 Isotopic evidence for a photolytically driven dynamic equilibrium in summer. *Atmos.*
977 *Chem. Phys.*, 13, 6403-6419, doi:10.5194/acp-13-6403-2013, 2013.
978
979 Erbland, J., Savarino, J., Morin, S., France, J.L., Frey, M.M., King, M.D.: Air-snow
980 transfer of nitrate on the East Antarctic plateau – Part 2: An isotopic model for the
981 interpretation of deep ice-core records. *Atmos. Chem. Phys. Discuss.*, 15,6886-6966,
982 doi:10.5194/acpd-15-6887-2015, 2015.
983
984 Fegyveresi, J.M., Alley, R.B., Spencer, M.K., Fitzpatrick, J.J., Steig, E.J., White, J.W.C.,
985 McConnell, J.R., Taylor, K.C.: Late-Holocene climate evolution at the WAIS Divide site,
986 West Antarctica: bubble number-density estimates. *J. Glaciol.*, 57, 204, 2011.
987
988 Fisher, J.A., Jacob, D.J., Wang, Q., Bahreini, R., Carouge, C.C., Cubison, M.J., Dibb,
989 J.E., Diehl, T., Jimenez, J.L., Leibensperger, E.M., Meinders, M.B.T., Pye, H.O.T.,
990 Quinn, P.K., Sharma, S., van Donkelaar, A., Yantosca, R.M.: Sources, distribution, and
991 acidity of sulfate-ammonium aerosol in the Arctic in winter-spring, *Atmos. Environ.*, 45,
992 7301-7318, 2011.
993
994 France, J.L., King, M.D., Frey, M.M., Erbland, J., Picard, G., Preunkert, S., MacArthur,
995 A., Savarino, J.: Snow optical properties at Dome C (Concordia), Antarctica; implications
996 for snow emissions and snow chemistry of reactive nitrogen. *Atmos. Chem. Phys.*, 11,
997 9787-9801, doi:10.5194/acp-11-9787-2011, 2011.
998
999 Frey, M. M., Savarino, J., Morin, S., Erbland, J., and Martins, J. M. F.: Photolysis imprint
1000 in the nitrate stable isotope signal in snow and atmosphere of East Antarctica and
1001 implications for reactive nitrogen cycling. *Atmos. Chem. Phys.*, 9, 8681-8696, 2009.
1002
1003 Frey, M. M., Brough, N., France, J. L., Anderson, P.S., Traulle, O., King, M.D., Jones,
1004 A.E., Wolff, E.W., Savarino, J.: The diurnal variability of atmospheric nitrogen oxides
1005 (NO and NO₂) above the Antarctic Plateau driven by atmospheric stability and snow
1006 emissions. *Atmos. Chem. Phys.*, 13, 3045-3062, doi:10.5194/acp-13-3045-2013, 2013.

- 1007
1008 Freyer, H. D., Kley, D., Voiz-Thomas, A., Kobel, K.: On the interaction of isotopic
1009 exchange processes with photochemical reactions in atmospheric oxides of nitrogen. *J.
1010 Geophys. Res. Atmos.*, 98(D8), 14791-14796, 1993.
1011
1012 Gallet, J.-C., Domine, F., Arnaud, L., Picard, G., and Savarino, J.: Vertical profiles of the
1013 specific surface area and density of the snow at Dome C and on a transect to Dumont
1014 D'Urville, Antarctica – albedo calculations and comparison to remote sensing products.
1015 *The Cryosphere.*, 5, 631-649, doi: 10.5194/tc-5-631-2011, 2011.
1016
1017 Geng, L., Alexander, B., Cole-Dai, J., Steig, E.J., Savarino, J., Sofen, E.D., Schauer, A.J.:
1018 Nitrogen isotopes in ice core nitrate linked to anthropogenic atmospheric acidity change.
1019 *Proc. Natl. Acad. Sci.*, 111, 16, 5808-5812, doi:10.1073/pnas.1319441111, 2014a.
1020
1021 Geng, L., Cole-Dai, J., Alexander, B., Erbland, J., Savarino, J., Schauer, A. J., Steig, E.J.,
1022 Lin, P., Fu, Q., Zatko, M.C.: On the origin of the occasional springtime nitrate
1023 concentration maximum in Greenland. *Snow. Atmos. Chem. Phys.*, 14, 13361-13376,
1024 doi:10.5194/acp-14-13361-2014, 2014b.
1025
1026 Geng, L., Zatko, M.C., Alexander, B., Fudge, T.J., Schauer, A.J., Murray, L.T., Mickley,
1027 L.J.: Effects of post-depositional processing on nitrogen isotopes of nitrate in the
1028 Greenland Ice Sheet Project 2 (GISP2) ice core. *Geophys. Res. Lett.*,
doi:10.1002/2015GL064218, 2015.
1029
1030 Grannas, A. M., Jones, A. E., Dibb, J., Ammann, M., Anastasio, C., Beine, H. J., Bergin,
1031 M., Bottenheim, J., Boxe, C. S., Carver, G., Chen, G., Crawford, J. H., Domine, F., Frey,
1032 M. M., Guzman, M. I., Heard, D. E., Helmig, D., Hoffman, M. R., Honrath, R. E., Huey,
1033 L. G., Hutterli, M., Jacobi, H. W., Klan, P., Lefer, B., McConnell, J., Plane, J., Sander,
1034 R., Savarino, J., Shepson, P. B., Simpson, W. R., Sodeau, J. R., von Glasow, R., Weller,
1035 R., Wolff, E. W., Zhu, T.: An overview of snow photochemistry: evidence, mechanisms
and impacts. *Atmos. Chem. Phys.*, 7, 4329-4373, 2007.
1036
1037 Grenfell, T. C.: A Radiative Transfer Model for Sea Ice With Vertical Structure
1038 Variations. *J. Geophys. Res.*, 96, 16991-17001, 1991.
1039
1040 Grenfell, T.C., Warren, S.G, Mullen, P.C.: Reflection of solar radiation by the Antarctic
1041 snow surface at ultraviolet, visible, and near-infrared wavelengths. *J. Geophys. Res.*, 99,
1042 18669-18684, 1994.
1043
1044 Handorf, D., Foken, T., Kottmeier, C.: The stable atmospheric boundary layer over an
1045 Antarctic ice sheet. *Boundary-Layer Meteorol*, 91, 165-189, 1999.
1046
1047 Hastings, M.G., Sigman, D.M., Steig, E.J.: Glacial/interglacial changes in the isotopes of
1048 nitrate from the Greenland Ice Sheet Project (GISP2) ice core. *Global Biogeochem.
1049 Cycles*, 19:GB4024, doi:10.1029/2005GB002502, 2005.
1050

- 1051 Heaton, T. H. E., Spiro, B., Robertson, M. C. S.: Potential canopy influences on the
1052 isotopic composition of nitrogen and sulphur in atmospheric deposition. *Oecologia*, 109,
1053 4, 600-607, 1997.
- 1054
- 1055 Helmig, D., Johnson, B., Oltmans, S.J., Neff, W., Eisele, F., Davis, D.: Elevated ozone in
1056 the boundary layer at South Pole. *Atmos. Environ.*, 42, 2788-2803, 2008.
- 1057
- 1058 Holtslag, A.A.M., Boville, B.: Local versus nonlocal boundary layer diffusion in a global
1059 climate model. *J. Clim.*, 6, 1825–1842, 1993.
- 1060
- 1061 Hudman, R.C., N.E. Moore, R.V. Martin, A.R. Russell, A.K. Mebust, L.C. Valin, and
1062 R.C. Cohen, A mechanistic model of global soil nitric oxide emissions: implementation
1063 and space based-constraints, *Atmos. Chem. Phys.*, 12, 7779-7795, doi:10.5194/acp-12-
1064 7779-2012, 2012.
- 1065
- 1066 Jarvis, J. C.: Isotopic studies of ice core nitrate and atmospheric nitrogen oxides in polar
1067 regions. Ph.D. Thesis, University of Washington, publication number 3328411, 2008.
- 1068
- 1069 Jin, Z., Charlock, T.P., Yang, P., Xie, Y., Miller, W.: Snow optical properties for
1070 different particle shapes with application to snow grain size retrieval and MODIS/CERES
1071 radiance comparison over Antarctica. *Remote. Sens. Environ.*, 112, 3563-3581, 2008.
- 1072
- 1073 Jones, A., Weller, R., Anderson, P., Jacobi, H., Wolff, E., Schrems, O., Miller, H.:
1074 Measurements of NO_x emissions from the Antarctic snowpack. *Geophys. Res. Lett.*, 28,
1075 1499-1502, doi: 10.1029/2000GL011956, 2001.
- 1076
- 1077 Jones, A.E., Anderson, P.S., Wolff, E.W., Turner, J., Rankin, A.M., Colwell, S.R.: A role
1078 for newly forming sea ice in springtime polar tropospheric ozone loss? Observational
1079 evidence from Halley station, Antarctica. *J. Geophys. Res.*, 111, D08306,
1080 doi:10.1029/2005JD006566, 2006.
- 1081
- 1082 Jones, A.E., Wolff, E.W., Salmon, R.A., Bauguitte, S.J.-B., Roscoe, H.K., Anderson,
1083 P.S., Ames, D., Clemitsshaw, K.C., Fleming, Z.L., Bloss, W.J., Heard, D.E., Lee, J.D.,
1084 Read, A.K., Hamer, P., Shallcross, D.E., Jackson, A.V., Walker, S.L., Lewis, A.C.,
1085 Mills, G.P., Plane, J.M.C., Saiz-Lopez, A., Sturges, W.T., Worton, D.R.: Chemistry of
1086 the Antarctic Boundary Layer and the Interface with Snow: an overview of the
1087 CHABLIS campaign. *Atmos. Chem. Phys.*, 8, 3789-3803, 2008.
- 1088
- 1089 Jones, A.E., Wolff, E.W., Ames, D., Bauguitte, S. J.-B., Clemitsshaw, K.C., Fleming, Z.,
1090 Mills, G.P., Saiz-Lopez, A., Salmon, R.A., Sturges, W.T., Worton, D.R.: The multi-
1091 seasonal NO_y budget in coastal Antarctica and its link with surface snow and ice core
1092 nitrate: results from the CHABLIS campaign. *Atmos. Chem. Phys.*, 11, 9271-9285,
1093 doi:10.5194/acp-11-9271, 2011, 2011.
- 1094

- 1095 King, J.C., Argentini, S.A., Anderson, P.S.: Contrasts between the summertime surface
1096 energy balance and boundary layer structure at Dome C and Halley stations, Antarctica.
1097 *J. Geophys. Res.*, 111, D02105, doi:10.1029/2005JD006130, 2006.
- 1098
- 1099 Klein, K.: Variability in dry Antarctic firn; Investigations on spatially distributed snow
1100 and firn samples from Dronning Maud Land, Antarctica. Ph.D. Thesis, Universitat
1101 Bremen. hdl: 10013/epic.44893. <http://nbn-resolving.de/urn:nbn:de:gbv:46-00104117-15>,
1102 date last access: April 15, 2014.
- 1103
- 1104 Kodama, Y., Wendler, G., Ishikawa, N.: The diurnal variation of the boundary layer in
1105 summer in Adelie Land, Eastern Antarctica. *J. Appl. Met.*, 28, 16-24, 1989.
- 1106
- 1107 Konig-Langlo, G., King, J., Pettre, P., Climatology of the three coastal Antarctic stations
1108 Dumont D'urville, Neumayer, and Halley. *J. Geophys. Res.*, D9, 103, 10935-10946,
1109 1998.
- 1110
- 1111 Lee, H., Henze, D.K., Alexander, B., Murray, L.T.: Investigating the sensitivity of
1112 surface-level nitrate seasonality in Antarctica to primary sources using a global model.
1113 *Atmos. Environ.*, 89, 757-767, doi:10.1016/j.atmosenv.2014.03.003, 2014.
- 1114
- 1115 Legrand, M.R., Kirchner, S.: Origins and variations of nitrate in South Polar
1116 precipitation. *J. Geophys. Res.*, 95, 3493-3507, 1990.
- 1117
- 1118 Levy, H., Moxim, W.J., Klonecki, A.A., Kasibhatla, P.S.: Simulated tropospheric NOx:
1119 Its evaluation, global distribution and individual source contributions. *J. Geophys. Res.*,
1120 104, 26279-26306, 1999.
- 1121
- 1122 Libois, Q., Picard, G., France, J. L., Arnaud, L., Dumont, M., Carmagnola, C. M., King,
1123 M. D.: Grain shape influence on light extinction in snow. *The Cryosphere*, 7, 1803-1818,
1124 doi:10.5194/tc-7-1803-2013, 2013.
- 1125
- 1126 Lin, S.J., Rood, R.B.: Multidimensional flux form semi-Lagrangian transport schemes.
1127 *Mon. Wea. Rev.*, 124, 2046-2070, 1996.
- 1128
- 1129 Lin, J. T., McElroy, M.B.: Impacts of boundary layer mixing on pollutant vertical profiles
1130 in the lower troposphere: Implications to satellite remote sensing. *Atmos. Environ.*, 44,
1131 1726-1749, doi:10.1016/j.atmosenv.2010.02.009, 2010.
- 1132 Liu, H., Jacob, D.J., Bey, I., Yantosca, R.M.: Constraints from ^{210}Pb and ^7Be on wet
1133 deposition and transport in a global three-dimensional chemical tracer model driven by
1134 assimilated meteorological fields, *J. Geophys. Res.*, 106(D11), 12,109-112,128, 2001.
- 1135 Logan, J.A., Nitrogen oxides in the troposphere: Global and regional budgets. *J.*
1136 *Geophys. Res.*, 88(C15), 10785-10807, doi:10.1029/JC088iC15p10785, 1983.
- 1137
- 1138 Mack, J., and Bolton, J. R.: Photochemistry of nitrite and nitrate in aqueous solution: A
1139 review. *J. Photochem. Photobiol. A.*, 128, 1-13, 1999.
- 1140

- 1141 Mao, J., Jacob, D.J., Evans, M.J., Olson, J.R., Ren, X., Brune, W.H., St. Clair, J.M.,
1142 Crounse, J. D., Spencer, K.M., Beaver, M.R., Wennberg, P.O., Cubison, M.J., Jimenez,
1143 J.L., Fried, A., Weibring, P., Walega, J.G., Hall, S.R., Weinheimer, A.J., Cohen, R.C.,
1144 Chen, G., Crawford, J.H., Jaegle, L., Fisher, J.A., Yantosca, R.M., Le Sager, P., Carouge,
1145 C.: Chemistry of hydrogen oxide radicals (HO_x) in the Arctic troposphere in spring.
1146 *Atmos. Chem. Phys.*, 10, 5823-5838, doi:10.5194/acp-10-5823-2010, 2010.
- 1147
- 1148 Masclin, S., Frey, M. M., Rogge, W. F., Bales, R. C.: Atmospheric nitric oxide and ozone
1149 at the WAIS Divide deep coring site: a discussion of local sources and transport in West
1150 Antarctica. *Atmos. Chem. Phys.*, 13, 8857-8877, doi:10.5194/acp-13-8857-2013, 2013.
- 1151
- 1152 Mayewski, P. A., and Legrand, M. R.: Recent increase in nitrate concentration of
1153 Antarctic snow. *Nature*, 346, 258-260, 1990.
- 1154
- 1155 Meusinger, C., Berhanu, T.A., Erbland, J., Savarino, J., Johnson, M.S.: Laboratory study
1156 of nitrate photolysis in Antarctic snow. I. Observed quantum yield, domain of photolysis,
1157 and secondary chemistry. *J. Chem. Phys.*, 140, 244305, doi:10.1063/1.4882898, 2014.
- 1158
- 1159 Morin, S., Savarino, J., Frey, M.M., Domine, F., Jacobi, H.-W., Kaleschke, L., Martins,
1160 J.M.F.: Comprehensive isotopic composition of atmospheric nitrate in the Atlantic Ocean
1161 boundary layer from 65°S to 79°N. *J. Geophys. Res.*, 114, D05303,
1162 doi:10.1029/208JD010696, 2009.
- 1163
- 1164 Mulvaney, R., Wagenbach, D., Wolff, E.W.: Postdepositional change in snowpack nitrate
1165 from observation of year-round near-surface snow in coastal Antarctica. *J. Geophys. Res.*,
1166 103, 11021-11031, 1998.
- 1167
- 1168 Murray, L.T., Jacob, D.J., Logan, J.A., Hudman, R.C., Koshak, W.J.: Optimized regional
1169 and interannual variability of lightning in a global chemical transport model constrained
1170 by LIS/OTD satellite data, *J. Geophys. Res.*, 117, D20307, 2012.
- 1171 Neff, W., Helmig, D., Grachev, A., Davis, D.: A study of boundary layer behaviour
1172 associated with high concentrations at the South Pole using a minisoder, tethered balloon,
1173 and a sonic anemometer. *Atmos. Environ.*, 42, 2762-2779, doi:10.1029/2012JD017934,
1174 2008.
- 1175
- 1176 Oliver, J.G.J., Van Aardenne, J.A., Dentener, F.J., Pagliari, V., Ganzeveld, L.N., Peters,
1177 J.A.H.W.: Recent trends in global greenhouse gas emissions: regional trends 1970-2000
1178 and spatial distribution of key sources in 2000. *Env. Sci.*, 2(2-3), 81-99,
1179 doi:10.1080/15693430500400345, 2005.
- 1180
- 1181 Oncley, S., Buhr, M., Lenschow, D., Davis, D., Semmer, S.: Observations of summertime
1182 NO fluxes and boundary-layer height at the South Pole during ISCAT 2000 using scalar
1183 similarity. *Atmos. Environ.*, 38, 5389-5398, doi:10.1016/j.atmosevn.2004.05.053, 2004.
- 1184

- 1185 Parish, T. R., and D. H. Bromwich (2007), Reexamination of the near-surface airflow
1186 over the Antarctic continent and implications on atmospheric circulations at high
1187 southern latitudes, *Monthly Weather Review*, 135, 1961-1973.
- 1188
- 1189 Parrella, J.P., Jacob, D.J., Liang, Q., Zhang, Y., Mickley, L.J., Miller, B., Evans, M.J.,
1190 Yang, X., Pyle, J.A., Theys, N., Van Roozendael, M.: Tropospheric bromine chemistry:
1191 implications for present and pre-industrial ozone and mercury. *Atmos. Chem. Phys.*, 12,
1192 6723-6740, doi:10.5194/acp-12-6723-2012, 2012.
- 1193
- 1194 Pratt, K. A., Custard, K. D., Shepson, P. B., Douglas, T. A., Pohler, D., General, S.,
1195 Zielcke, J., Simpson, W. R., Platt, U., Tanner, D. J., Huey, L. G., Carlsen, M., Stirm, B.
1196 H.: Photochemical production of molecular bromine in Arctic surface snowpacks.
1197 *Nature*, 6, 351-356, doi:10.1038/NGEO1779, 2013.
- 1198
- 1199 Price, C., Rind, D.: A simple lightning parameterization for calculating global lightning
1200 distributions. *J. Geophys. Res.*, 97, 9919–9933, 1992.
- 1201
- 1202 Rothlisberger, R., Hutterli, M. A., Sommer, S., Wolff, E. W., and Mulvaney, R.: Factors
1203 controlling nitrate in ice cores: Evidence from the Dome C deep ice core. *J. Geophys.*
1204 *Res.*, 105, 20565-20572, 2000.
- 1205
- 1206 Sander, S. P., Friedl, R.R., Golden, D.M., Kurylo, M.J., Moortgat, G.K., Keller-Rudek,
1207 H., Wine, P.J., Ravishankara, A.R., Kolb, C.E., Molina, M.J., Finalyson-Pitts, B.J., Huie,
1208 R.E., Orkin, V.L.: Chemical kinetics and photochemical data for use in atmospheric
1209 studies evaluation number 15. JPL Publications, Pasadena, 1-523, 06-2, 2006.
- 1210
- 1211 Savarino, J., Kaiser, J., Morin, S., Sigman, D.M., Thiemens, M.H.: Nitrogen and oxygen
1212 isotopic constraints on the origin of atmospheric nitrate in coastal Antarctica. *Atmos.*
1213 *Chem. Phys.*, 7, 1925-1945, 2007.
- 1214
- 1215 Simpson, W. R., von Glasow, R., Riedel, K., Anderson, P., Ariya, P., Bottenheim, J.,
1216 Burrows, J., Carpenter, L. J., Friess, U., Goodsite, M. E., Heard, D., Hutterli, M., Jacobi,
1217 H.-W., Kaleschke, L., Neff, B., Plane, J., Platt, U., Richter, A., Roscoe, H., Sander, R.,
1218 Shepson ,P., Sodeau, J., Steffen, A., Wagner, T., Wolff, E.: Halogens and their role in
1219 polar boundary-layer ozone depletion. *Atmos. Chem. Phys.*, 7(16):4375–4418, 2007.
- 1220
- 1221 Slusher, D. L., Huey, L. G., Tanner, D. J., Chen, G., Davis, D. D., Buhr, M., Nowak, J.
1222 B., Eisele, F. L., Kosciuch, E., Mauldin, R. L., Lefer, B. L., Shetter, R. E., Dibb, J. E.:
1223 Measurements of pernitric acid at the South Pole during ISCAT 2000. *Geophys. Res.*
1224 *Lett.*, 29, 21, doi:10.1029/2002GL015703, 2002.
- 1225
- 1226 Shi, G., Buffen, A.M., Hastings, M.G., Li, C., Ma, H., Li, Y., Sun, B., An, C., Jiang, S.:
1227 Investigation of post-depositional processing of nitrate in East Antarctica snow: isotopic
1228 constraints on photolytic loss, re-oxidation, and source inputs. *Atmos. Chem. Phys.*
1229 *Discuss.*, 14, 31943-31986, doi: 10.5194/acpd-14-31943-2014, 2014.
- 1230

- 1231 Sjostedt, S.J., Huey, L.G., Tanner, D.J., Peischl, J., Chen, G., Dibb, J.E., Lefer, B.,
1232 Hutterli, M.A., Beyersdorf, A.J., Blake, N.J., Blake, D.R., Sueper, D., Ryerson, T.,
1233 Burkhardt, J., Stohl, A.: Observations of hydroxul and the sum of peroxy radicals at
1234 Summit, Greenland during summer 2003. *Atmos. Environ.*, 41, 5122-5137, 2007.
1235
- 1236 Sofen, E.D., Alexander, B., Steig, E.J., Thiemens, M.H., Kunasek, S.A., Amos, H.M.,
1237 Schauer, A.J., Hastings, M.G., Bautista, J., Jackson, T.L., Vogel, L.E., McConnell, J.R.,
1238 Pasteris, D.R., Saltzman, E.S.: WAIS Divide ice core suggests sustained changes in the
1239 atmospheric formation pathways of sulfate and nitrate since the 19th century in the
1240 extratropical Southern Hemisphere. *Atmos. Chem. Phys.*, 14, 5749-5769,
1241 doi:10.5194/acp-14-5749-2014, 2014.
1242
- 1243 Thomas, J. L., Dibb, J. E., Huey, L. G., Liao, J., Tanner, D., Lefer, B., von Glasow, R.,
1244 Stutz, J.: Modeling chemistry in and above snow at Summit, Greenland – Part 2: Impact
1245 of snowpack chemistry on the oxidation capacity of the boundary layer. *Atmos. Chem.
1246 Phys.*, 12, 6537-6554, doi:10.5194/acp-12-6537-2012, 2012.
1247
- 1248 Thompson, A.M., The oxidizing capacity of the Earth's atmosphere: Probable past and
1249 future changes. *Science*, 256, 1157-1165, 1992.
1250
- 1251 Travouillon, T., Ashley, M.C.B., Burton, M.G., Storey, J.W.V., Loewenstein, R.F.:
1252 Atmospheric turbulence at the South Pole and its implications for astronomy. *Astronom.
1253 And Astrophys.*, 400, 1163-1172, doi:10.1051/0004-6361:20021814, 2003.
1254
- 1255 UNEP/WMO. Integrated Assessment of Black Carbon and Tropospheric Ozone:
1256 Summary for Decision Makers, UNON/Publishing Services Section/Nairobi, ISO
1257 14001:2004, 2011.
1258
- 1259 van Donkelaar, A., R. V. Martin, W. R. Leaitch, A.M. Macdonald, T. W. Walker, D. G.
1260 Streets, Q. Zhang, E. J. Dunlea, J. L. Jimenez, J. E. Dibb, L. G. Huey, R. Weber, and M.
1261 O. Andreae. Analysis of Aircraft and Satellite Measurements from the Intercontinental
1262 Chemical Transport Experiment (INTEX-B) to Quantify Long-Range Transport of East
1263 Asian Sulfur to Canada. *Atmos. Chem. Phys.*, 8, 2999-3014, 2008.
1264
- 1265 van der Werf, G.R, Morton, D.C., DeFries, R.S., Giglio, L., Randerson, J.T., Collatz,
1266 G.J., Kasibhatla, P.S.: Estimates of fire emissions from an active deforestation region in
1267 the southern Amazon based on satellite data and biogeochemical
1268 modeling. *Biogeosciences*, 6 (2):235-249, 2009.
1269
- 1270 Wagenbach, D., Legrand, M., Fischer, H., Pichlmayer, F., Wolff, E.W.: Atmospheric
1271 near-surface nitrate at coastal Antarctic sites. *J. Geophys. Res.*, 103, 11007-11020, 1998.
1272
- 1273 Wang, Y. H., Jacob, D.J., Logan, J.A.: Global simulation of tropospheric O₃-NO_x
1274 hydrocarbon chemistry 1. Model formulation, *J. Geophys. Res.*, 103, 10,713-710,725,
1275 1998.
1276

- 1277 Wang, Y., Choi, Y., Zeng, T., Davis, D., Buhr, M., Huey, G. L., and Neff, W.: Assessing
1278 the photochemical impact of snow NO_x emissions over Antarctica during ANTCI 2003.
1279 *Atmos. Environ.*, 41, 3944-3958, doi:10.1016/j.atmosenv.2007.01.056, 2008.
- 1280
- 1281 Wang, Q., Jacob, D.J., Fisher, J.A., Mao, J., Leibensperger, E.M., Carouge, C.C., Le
1282 Sager, P., Kondo, Y., Jimenez, J. L., Cubison, M. J., Doherty, S.: Sources of
1283 carbonaceous aerosols and deposited black carbon in the Arctic in winter-spring:
1284 implications for radiative forcing. *Atmos. Chem. Phys.*, 11, 12453-12473,
1285 doi:10.5194/acp-11-12453-2011, 2011.
- 1286
- 1287 Warren, S.G., Clarke, A.D.: Soot in the atmosphere and snow surface of Antarctica. *J.*
1288 *Geophys. Res.*, 95, 1811-1816, 1990.
- 1289
- 1290 Warren, S. G., Brandt, R. E., and Grenfell, T. C.: Visible and near-ultraviolet absorption
1291 spectrum of ice from transmission of solar radiation into snow. *Appl. Opt.*, 45, 5320-
1292 5334, 2006.
- 1293
- 1294 Weller, R., Minikin, A., Konig-Langlo, G., Schrems, O., Jones, A.E., Wolff, E.W.,
1295 Anderson, P.S.: Investigating possible causes of the observed diurnal variability in
1296 Antarctica NO_y. *Geophys. Res. Lett.*, 26, 18, 2853-2856, 1999.
- 1297
- 1298 Wesely, M. L.: Parameterization of surface resistances to gaseous dry deposition in
1299 regional-scale numerical-models, *Atmos. Env.*, 23, 1293-130, 1989.
- 1300
- 1301 Wild, O., Q. Zhu, and M. J. Prather (2000), Fast-J: Accurate simulation of in- and below-
1302 cloud photolysis in global chemical models, *J. Atm. Chem.*, 37, 245-282.
- 1303
- 1304 Wolff, E.W.: Nitrate in polar ice, in *Ice Core Studies of Global Biogeochem. Cycles*,
1305 NATO ASI Ser., Ser. I, pp. 195-224, edited by R.J. Delmas, Springer, New York, 1995.
- 1306
- 1307 Wolff, E.W., Jones, A.E., Bauguitte, S. J.-B., Salmon, R.A.: The interpretation of spikes
1308 and trends in concentration of nitrate in polar ice cores, based on evidence from snow and
1309 atmospheric measurements. *Atmos. Chem. Phys.*, 8, 5627-5634, 2008.
- 1310
- 1311 Xu, L., Penner, J.E.: Global simulations of nitrate and ammonium aerosols and their
1312 radiative effects. *Atmos. Chem. Phys.*, 12, 9479-9504, doi:10.5194/acp-12-9479-2012,
1313 2012.
- 1314
- 1315 Zatko, M.C., Grenfell, T.C., Alexander, B., Doherty, S.J., Thomas, J.L., Yang, X., The
1316 influence of snow grain size and impurities on the vertical profiles of actinic flux and
1317 associated NO_x emissions on the Antarctic and Greenland ice sheets. *Atmos. Chem.*
1318 *Phys.*, 13, 3547-3567, doi:10.5194/acp-13-3547-2013, 2013.
- 1319
- 1320 Zatko, M.C. and Warren, S.G.: East Antarctic sea ice in spring: spectral albedo of snow,
1321 nilas, frost flowers, and slush; and light-absorbing impurities in snow. *Ann. Glaciol.*

- 1322 Special Issue: Sea ice in a changing environment, 56(69), 53-64,
1323 doi:10.3189/2015AoG69A574, 2015.
- 1324
- 1325 Zhang, L., S. Gong, J. Padro, and L. Barrie.: A size-segregated particle dry deposition
1326 scheme for an atmospheric aerosol module, *Atmos. Env.*, 35, 549-560, 2001.
- 1327
- 1328 Zhu, C., Xiang, B., Chu, L.T., Zhu, L.: 308 nm Photolysis of Nitric Acid in the Gas
1329 Phase, on Aluminum Surfaces, and on Ice Films. *J. Phys. Chem. A.*, 114, 2561-2568, doi:
1330 10.1021/jp909867a, 2010.
- 1331
- 1332
- 1333
- 1334
- 1335
- 1336
- 1337
- 1338
- 1339
- 1340
- 1341
- 1342
- 1343
- 1344
- 1345
- 1346
- 1347
- 1348
- 1349
- 1350
- 1351
- 1352
- 1353
- 1354
- 1355
- 1356
- 1357
- 1358
- 1359
- 1360
- 1361
- 1362
- 1363
- 1364
- 1365
- 1366
- 1367

1368 Table 1. Glossary of variables used in this paper.

Variable	Unit	Description
λ	nm	Wavelength
ϕ	molec photon ⁻¹	Quantum yield for NO ₃ ⁻ photolysis
$\sigma_{NO_3^-}$	cm ²	Absorption cross-section for NO ₃ ⁻ photolysis
I	photons cm ⁻² s ⁻¹ nm ⁻¹	Actinic flux of UV radiation
z_e	cm	e-folding depth of UV actinic flux in snow
z_{3e}	cm	Depth of snow photic zone
α_r	kg m ⁻² yr ⁻¹	Total annual snow accumulation rate
C_{BC}	ng g ⁻¹	Annual mean snow black carbon concentration
r_e	μm	Radiation equivalent mean ice grain radii
$K_{ext,tot}$	cm ⁻¹	Bulk extinction coefficient for snow
[NO ₃ ⁻] _{top}	ng g ⁻¹	Mean NO ₃ ⁻ concentration in top 2 cm of snow
[NO ₃ ⁻] _{bot}	ng g ⁻¹	Mean NO ₃ ⁻ concentration from 2-cm depth to the bottom of the snow photic zone
EF	unitless	NO ₃ ⁻ enhancement factor in top 2 cm of snow
F_p	fraction	Fraction of photolabile NO ₃ ⁻ in snow
$\Delta^{17}O(NO_3^-)$	‰	Oxygen isotopic composition of NO ₃ ⁻
$\delta^{15}N(NO_3^-)$	‰	Nitrogen isotopic composition of NO ₃ ⁻
ε	‰	Fractionation constant for NO ₃ ⁻ photolysis
F_{NO_x}	molec cm ⁻² s ⁻¹	Mean austral summer flux of snow-sourced NO _x
F_{NO_x}	ng N m ⁻² yr ⁻¹	Annual sum of snow-sourced NO _x flux
F_{PRI}	ng N m ⁻² yr ⁻¹	Annual sum of primary NO ₃ ⁻ deposited to snow
F_R	ng N m ⁻² yr ⁻¹	Annual sum of recycled NO ₃ ⁻ to snow
NRF_{yr}	unitless	Metric to assess degree of nitrogen recycling in 1 year
NRF_{τ_z}	unitless	Metric to assess degree of nitrogen recycling before NO ₃ ⁻ burial below snow photic zone
τ_z	years	Years NO ₃ ⁻ remains in snow photic zone
f	fraction	Fraction of photolysis-driven loss of NO ₃ ⁻ from snow

1369

1370

1371

1372

1373

1374

1375

1376

1377

1378

1379

1380

1381

1382

1383

1384

1385

1386

Table 2. Value(s) of parameters used in the model.

Variable	Value(s) used in model	References
ϕ	0.002 molec photon ⁻¹ ^a	Chu and Anastasio [2003]
$\sigma_{NO_3^-}$	2.7x10 ⁻²⁰ cm ² ($\lambda=298\text{-}307$ nm) 2.4x10 ⁻²⁰ cm ² ($\lambda=307\text{-}312$ nm) 1.9x10 ⁻²⁰ cm ² ($\lambda=312\text{-}320$ nm) 2.3x10 ⁻²¹ cm ² ($\lambda=320\text{-}345$ nm)	Sander et al. [2006]
ϵ	-47.9%	Berhanu et al. [2014]
r_e	Jan: 332.0 μm ^b Dec-Feb: 198-332.0 μm ^b Mar-Nov: 86.0-332.0 μm ^b	Gallet et al. [2011] Klein [2014]
ρ_{snow}	260-360 kg m ⁻³ ^c	Gallet et al. [2011]
EF^b	6 ^d	Dibb et al. [2004] Erbland et al. [2013] Frey et al. [2009] Mayewski and Legrand [1990] Rothlisberger et al. [2000]
$[NO_3^-]_{bot}$	60 ng g ⁻¹ ^e	Bertler et al. [2005]

^aAt temperature (T) = 244K^b r_e is varied vertically and temporally, but uniformly across Antarctica based on Gallet et al. [2011] and Klein [2014]. In January, r_e is constant with depth (332 μm), in December and February, r_e ranges from 198 μm at the snow surface to 332 μm at 300 cm depth, and from March to November, r_e ranges from 86 μm at the surface to 360 μm at 300 cm depth.^cThe mean vertical ρ_{snow} profile from several Dome C snowpits are used in this study (see Figure 11 in Gallet et al. [2011]).^dMedian of observed NO_3^- enhancement factors.^eMedian of observed sub-surface snow NO_3^- mixing ratios from the ITASE campaign.

1387

1388

1389

1390

1391

1392

1393

1394

1395

1396

1397

1398

1399

1400

1401

1402

1403

1404

1405

1406

1407

1408

1409

1410

1411

1412

1413

1414
 1415 Table 3. Dependence of mean austral summer (DJF) flux of snow-sourced NO_x ($\overline{F_{NOx}}$) on
 1416 quantum yield (ϕ), the fraction of photolabile NO₃⁻ (F_p), snow NO₃⁻ concentrations below
 1417 2 cm ($[NO_3^-]_{bot}$), the radiation equivalent ice grain radius (r_e), the bulk snow extinction
 1418 coefficient ($Kext_{tot}$), the NO₃⁻ concentration enhancement factor in the top 2 cm (EF), and
 1419 snow black carbon concentration (C_{BC}).

Parameter	Base case values ^a	Values used in sensitivity studies	$\overline{F_{NOx}}$ range in sensitivity studies ($\times 10^8$ molec $\text{cm}^{-2} \text{s}^{-1}$)	Correspor Figure
Quantum yield (ϕ)	0.002 molec photon ⁻¹ ^b	0.6 molec photon ⁻¹	5-2600	Fig. 4a, b, Fig. 1Aa
Fraction of photolabile NO ₃ ⁻ (F_p)	0.01-0.99 (spatial variation, Figure 3c)	Set to 1 everywhere	3.7-9.6	Fig. 4c, d
Sub-surface snow NO ₃ ⁻ ($[NO_3^-]_{bot}$)	60.0 ng g ⁻¹ ^c	30-120 ng g ⁻¹	0.3-15.8	Fig. 1Ab,
Radiation equivalent mean ice grain radii (r_e)	Jan: 332.0 μm ^d Dec-Feb: 198-332.0 μm ^d Mar-Nov: 86.0-332.0 μm ^d	Study 1: 332.0 μm ^e Study 2: 198-332.0 μm ^e Study 3: 86.0-332.0 μm ^e	0.5-10.2	Fig. 1Aj
Bulk snow extinction coefficient ($Kext_{tot}$)	$1.7-6.9 \times 10^3 \text{ m}^{-1}$ (spatial variation)	$\pm 20\%$ with respect to base case values	0.5-9.4	Fig. 1A
NO ₃ ⁻ enhancement factor in top 2 cm (EF)	6.0 ^f	1-10	0.5-9.3	Fig. 1A
Snow black carbon (C_{BC})	0.08-0.6 ng g ⁻¹ (spatial variation, Figure 3b)	\pm factor of 2 with respect to base case values	0.5-8.6	Fig. 1A

1420 ^abase case $F_{NOx}=0.5-7.8 \times 10^8$ molec $\text{cm}^{-2} \text{s}^{-1}$ (Figure 4d)

1421 ^bfrom Chu and Anastasio [2003] at T=244K

1422 ^cmedian of ITASE campaign [Bertler et al., 2005]

1423 ^d r_e is varied vertically and temporally, but uniformly across Antarctica based on Gallet et
 1424 al. [2011] and Klein [2014]. In January, r_e is constant with depth (332 μm), in December
 1425 and February, r_e ranges from 198 μm at the snow surface to 332 μm at 300 cm depth, and
 1426 from March to November, r_e ranges from 86 μm at the surface to 360 μm at 300 cm
 1427 depth.

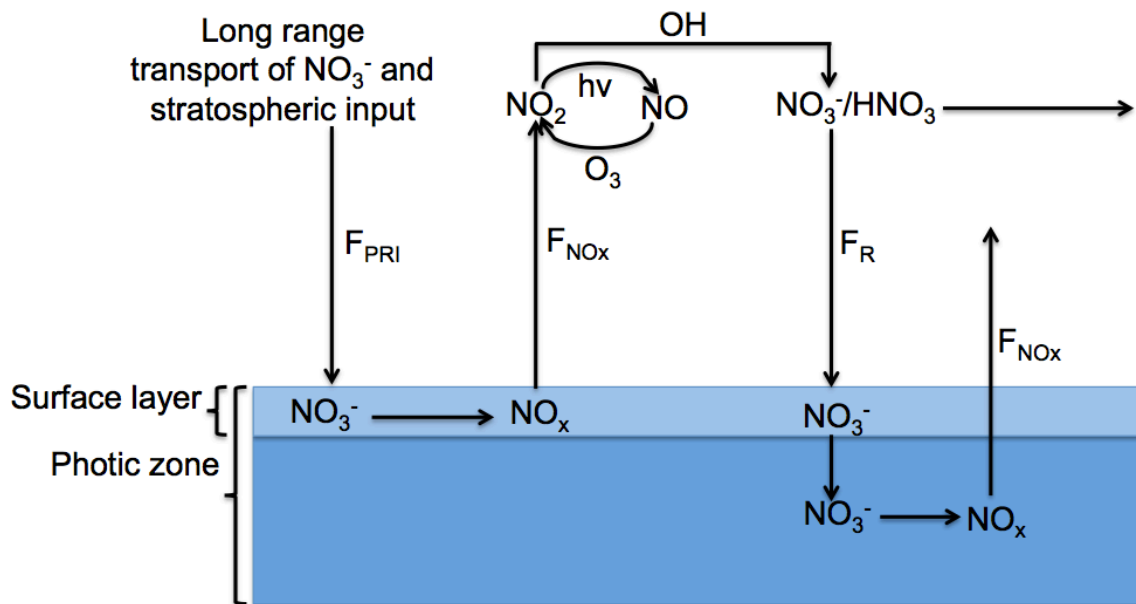
1428 ^ein r_e sensitivity study 1, the base-case ‘January’ r_e profile is applied for every month. In
 1429 r_e sensitivity study 2, the base-case ‘December and February’ r_e profile is applied for
 1430 every month. In r_e sensitivity study 3, the base-case ‘March-November’ r_e profile is
 1431 applied for every month.

1432 ^fmedian of observed EF [Dibb et al., 2004, Frey et al., 2009, Mayewski and Legrand,
 1433 1990, Rothlisberger et al., 2000].

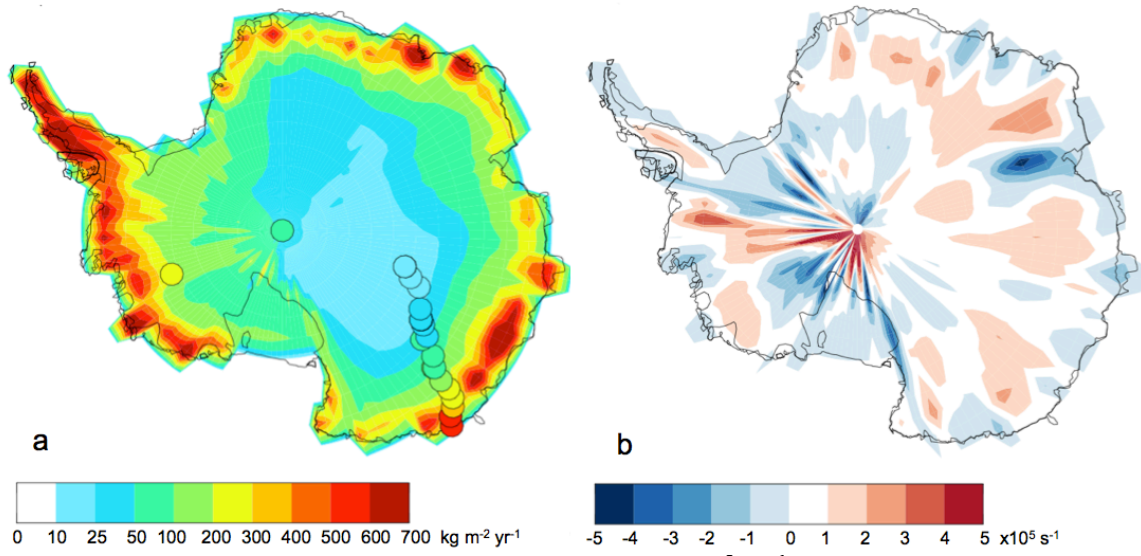
1434

1435

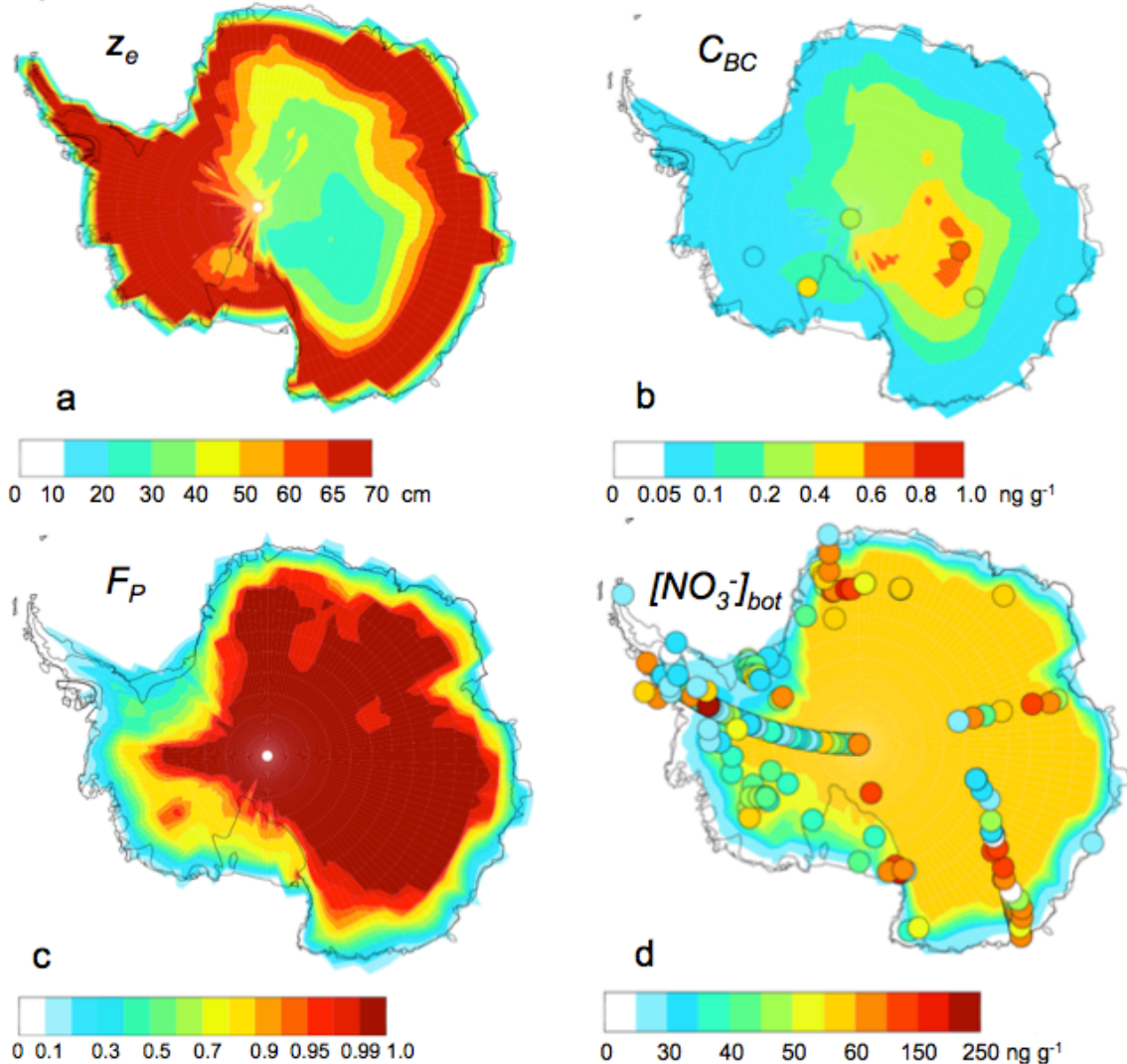
1436



1439 Figure 1. Schematic showing the nitrogen recycling associated with NO_3^- photolysis as
 1440 included in the model. F_{PRI} ($\text{ng N m}^{-2} \text{ yr}^{-1}$) is the downward, primary flux of NO_3^- to
 1441 Antarctica originating from long-range transport and the stratosphere, F_{NOx} ($\text{ng N m}^{-2} \text{ yr}^{-1}$)
 1442 is the upward flux of snow-sourced NO_x to the boundary layer, and F_R ($\text{ng N m}^{-2} \text{ yr}^{-1}$)
 1443 is downward, recycled flux of HNO_3 to the snow surface. The surface snow layer (top 2
 1444 cm) is distinguished from the rest of the photic zone because 30-65% of snow-sourced
 1445 NO_x is produced in the top 2 cm of snowpack [Zatko *et al.*, 2013], and because both NO_3^-
 1446 concentrations and actinic flux are much higher in the top surface layer compared to
 1447 deeper layers.



1454
 1455 Figure 2. (a) Annual total snow accumulation rate ($\text{kg m}^{-2} \text{yr}^{-1}$) in GEOS-Chem from May
 1456 2009 to May 2010 with annual snow accumulation rates (circles) estimated in Erbland et
 1457 al. [2013], Fegyveresi et al. [2011], and Grenfell et al. [1994]. (b) Annual mean surface
 1458 wind divergence (s^{-1}) in GEOS-Chem from May 2009 to May 2010. Blue regions indicate
 1459 regions of convergence.
 1460
 1461



1462
 1463 Figure 3. (a) Calculated mean austral summer (DJF) UV e-folding depth (z_e). (b)
 1464 Modeled and observed (circles) annual mean snow black carbon concentrations (C_{BC}),
 1465 with observations from WAIS-Divide and Law Dome [Bisiaux et al., 2013], Siple Dome
 1466 [Chylek et al., 1992], Vostok [Grenfell et al., 1994], South Pole [Warren and Clarke,
 1467 1990], and Dome C [Warren et al., 2006]. (c) Ratio of annual dry-deposited NO_3^- to
 1468 annual total deposited NO_3^- , F_P . (d) Annual sub-surface snow NO_3^- concentrations ($[\text{NO}_3^-]$
 1469 $_{\text{bot}}$) from 2-cm depth to the bottom of the snow photic zone (z_{3e}) used in the model scaled
 1470 by F_P . Mean sub-surface multi-year NO_3^- observations from the ITASE campaign along
 1471 with mean asymptotic (sub-photocline) NO_3^- mixing ratios from Erbland et al. [2013]
 1472 and Shi et al. [2014] (circles) are also included in Figure 3d [Bertler et al., 2005].
 1473
 1474
 1475
 1476
 1477
 1478
 1479

1480
1481

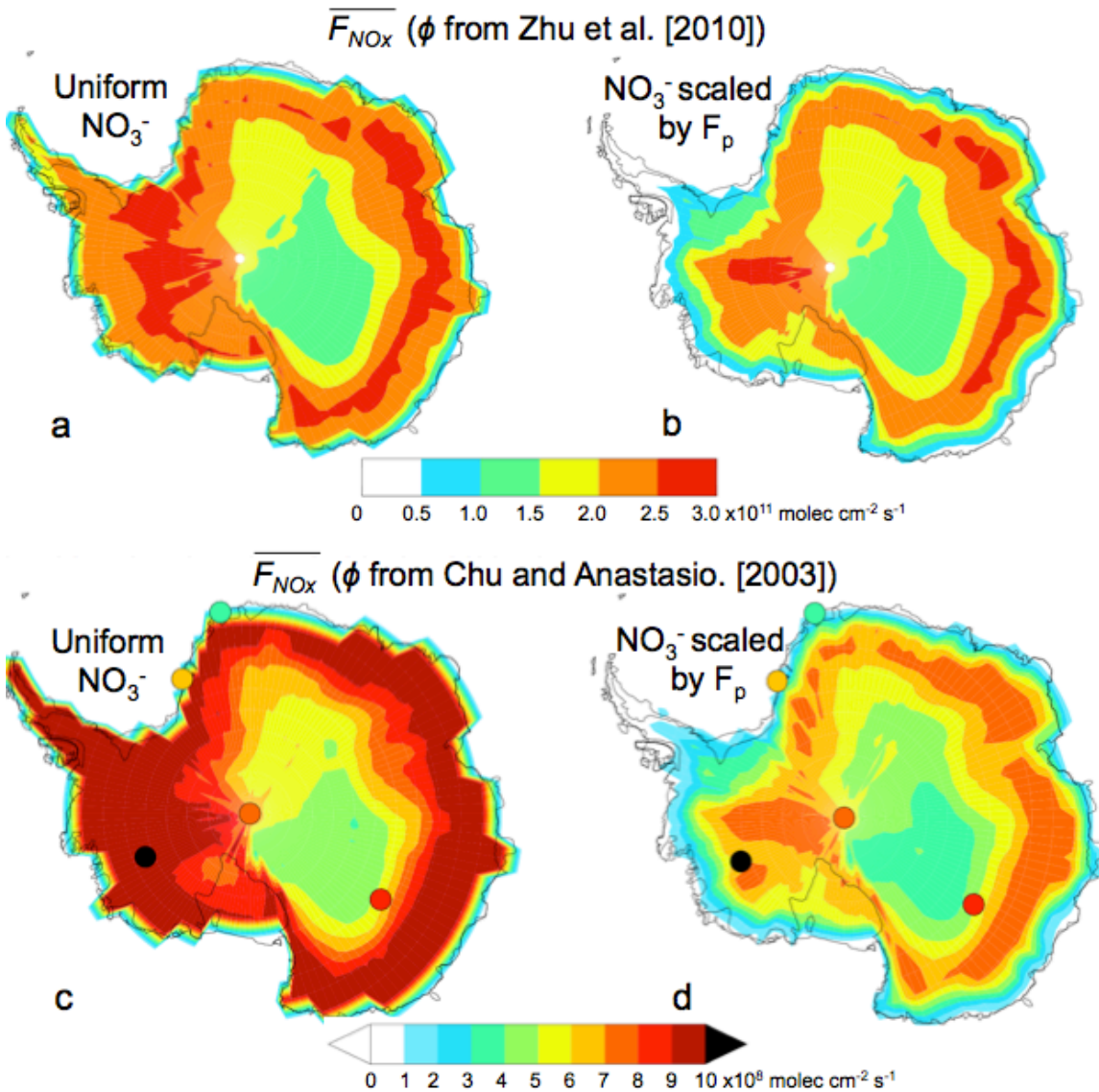
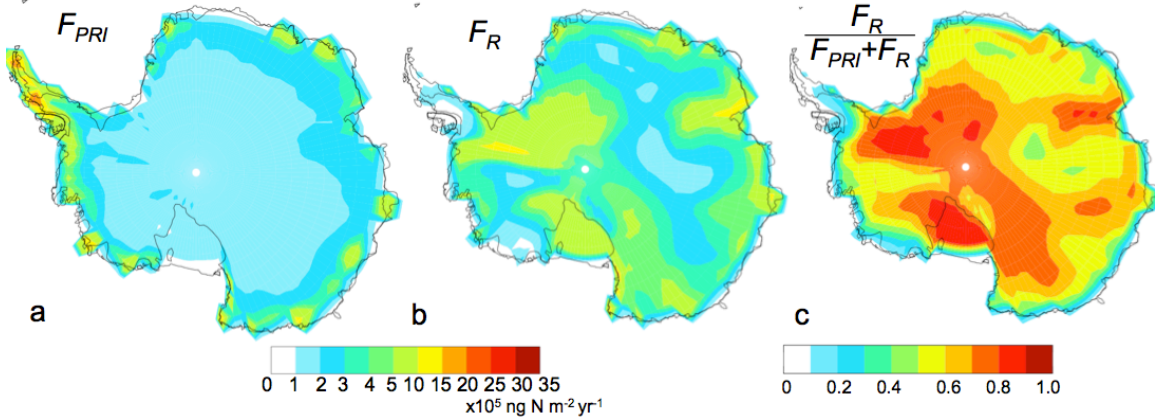


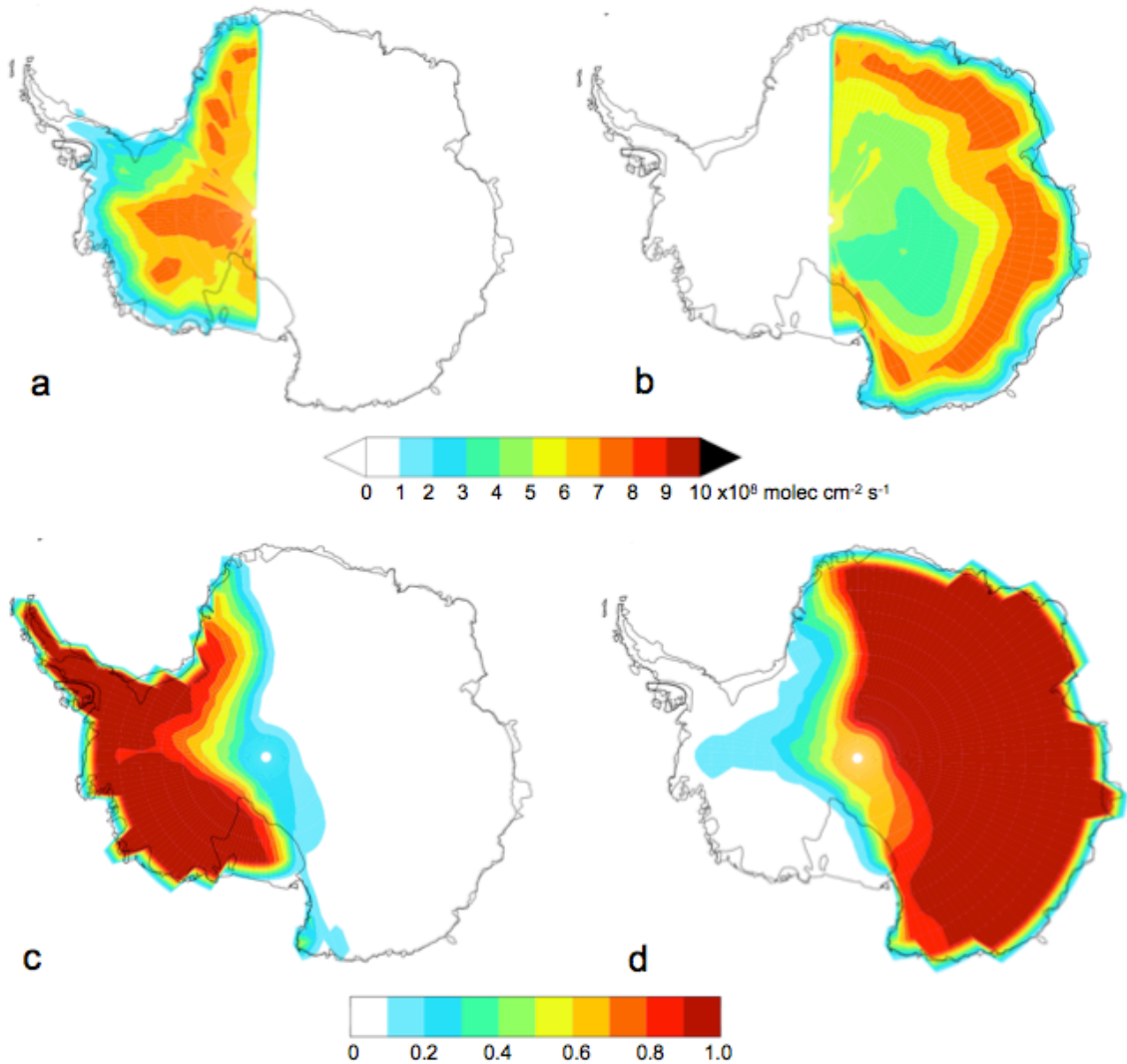
Figure 4. Mean austral summer (DJF) flux of snow-sourced NO_x from the snow ($\overline{F_{NOx}}$) with previously reported F_{NOx} observations from Neumayer [Jones et al., 2001], Halley [Jones et al., 2011, Bauguitte et al., 2012], South Pole [Oncley et al., 2004, Wang et al., 2008, Zatko et al., 2013], WAIS-Divide [Mascllin et al., 2013], and Dome C [Frey et al., 2013, Zatko et al., 2013]. (a) $\overline{F_{NOx}}$ calculated using ϕ from Zhu et al. [2010] and uniform snow NO_3^- concentrations ($[NO_3^-]_{top}=360 \text{ ng g}^{-1}$, $[NO_3^-]_{bot}=60 \text{ ng g}^{-1}$). (b) $\overline{F_{NOx}}$ calculated using ϕ from Zhu et al. [2010] and uniform snow NO_3^- concentrations ($[NO_3^-]_{top}=360 \text{ ng g}^{-1}$, $[NO_3^-]_{bot}=60 \text{ ng g}^{-1}$) scaled by the ratio of annual dry-deposited NO_3^- to annual total deposited NO_3^- (F_p , Figure 3c) (c) $\overline{F_{NOx}}$ calculated using ϕ from Chu and Anastasio [2003] and uniform snow NO_3^- concentrations ($[NO_3^-]_{top}=360 \text{ ng g}^{-1}$, $[NO_3^-]_{bot}=60 \text{ ng g}^{-1}$). (d) Base case: $\overline{F_{NOx}}$ calculated using ϕ from Chu and Anastasio [2003] and uniform snow NO_3^- concentrations ($[NO_3^-]_{top}=360 \text{ ng g}^{-1}$, $[NO_3^-]_{bot}=60 \text{ ng g}^{-1}$) scaled by the ratio of annual dry-deposited NO_3^- to annual total deposited NO_3^- (F_p).

1496
1497
1498
1499

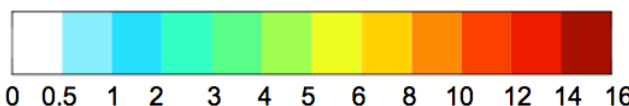
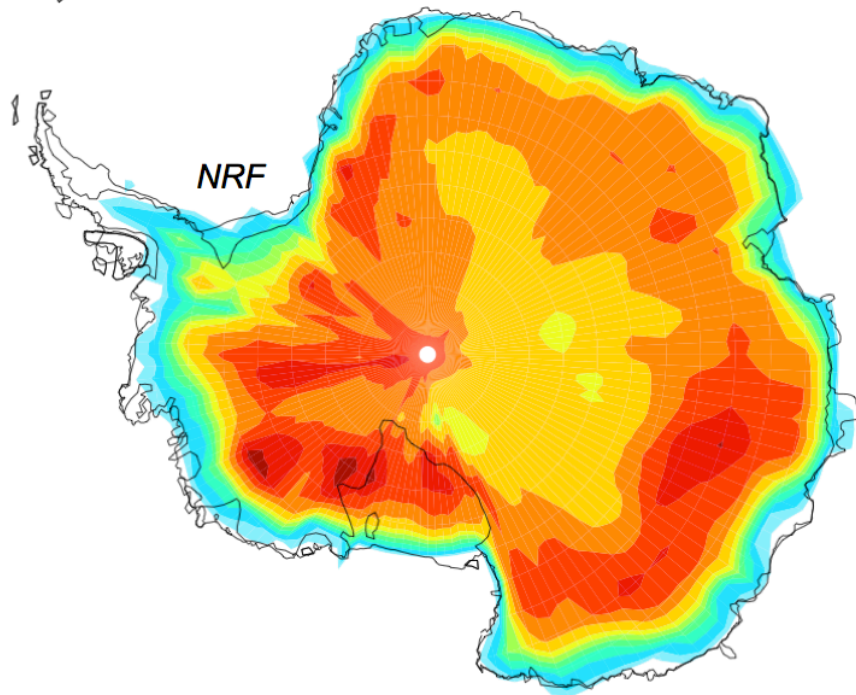


1500
1501 Figure 5. (a) Annual wet plus dry deposition flux of primary NO_3^- to the snow (F_{PRI}). (b)
1502 Annual wet plus dry deposition flux of recycled NO_3^- to the snow (F_R). (c) Ratio of F_R to
1503 the total downward NO_3^- flux ($\frac{F_R}{F_{PRI}+F_R}$) for the base case scenario.

1504
1505
1506
1507
1508
1509
1510
1511
1512
1513
1514
1515
1516



1517
 1518 Figure 6. Sensitivity studies examining transport of snow-sourced NO_x across Antarctica.
 1519
 1520 Mean austral summer (DJF) $\overline{F_{\text{NO}_x}}$ across Antarctica when $\overline{F_{\text{NO}_x}}$ set to 0 (a) in East
 1521
 1522 Antarctica and (b) in West Antarctica. Ratio of recycled NO_3^- flux (F_R) to F_R in the base
 1523
 1524 scenario when $F_{\text{NO}_x}=0$ in (c) East Antarctica and (d) in West Antarctica.
 1525
 1526



1527
1528 Figure 7. Nitrogen recycling factor (*NRF*, E8).

1529

1530

1531

1532

1533

1534

1535

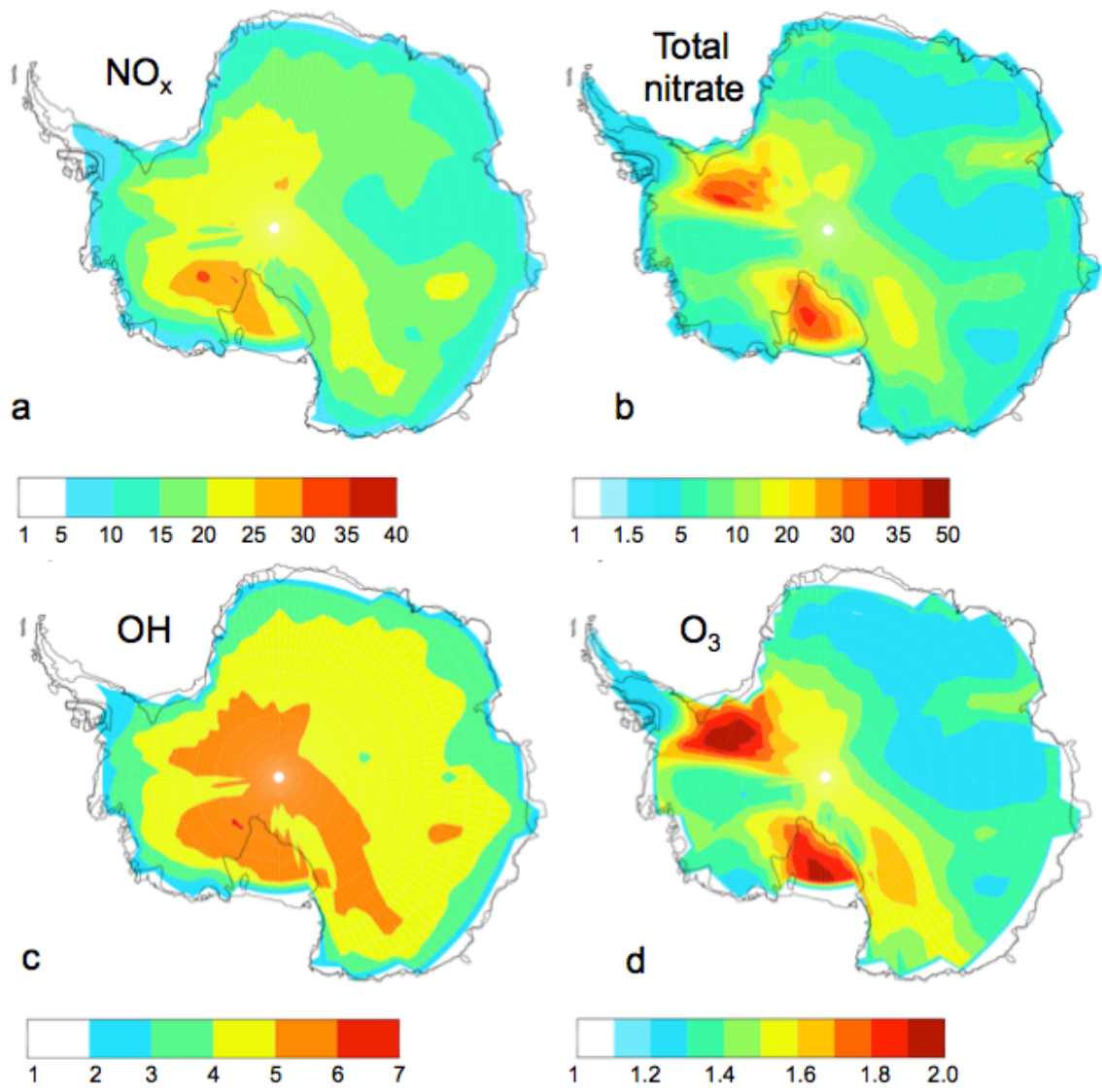
1536

1537

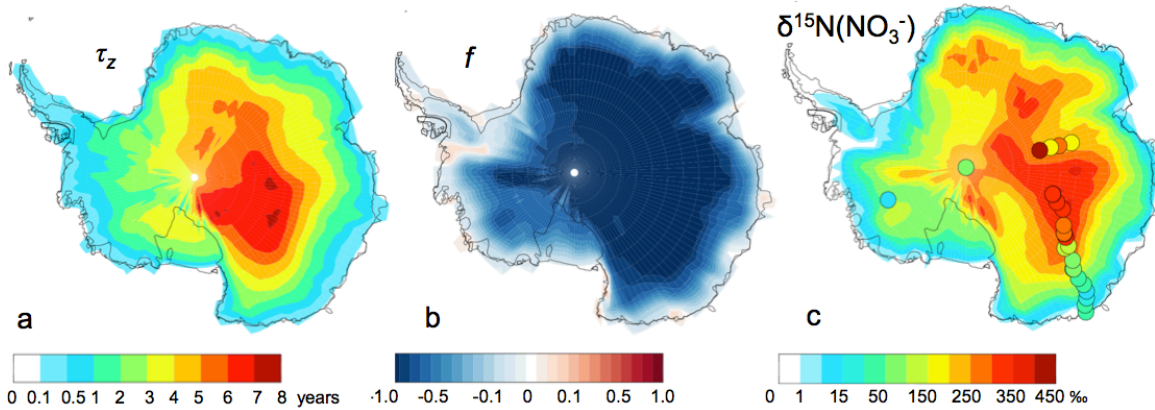
1538

1539

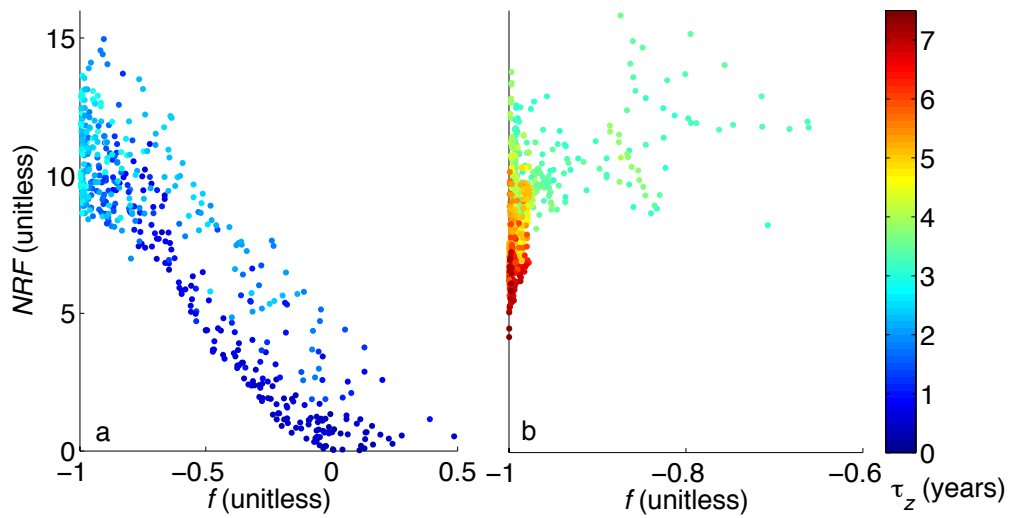
1540



1541
1542 Figure 8. Factor increase in mean austral summer (DJF) boundary layer (a) NO_x , (b)
1543 gas+aerosol phase nitrate, (c) OH, and (d) O_3 mixing ratios between model runs with
1544 F_{NO_x} compared to without F_{NO_x} .
1545
1546
1547
1548



1549
1550 Figure 9. (a) Minimum years NO_3^- remains in photolytic zone (τ_z , years, E10). (b)
1551
1552 Fraction of NO_3^- gained (positive values) or lost (negative values) from the snow through
1553 photolysis (f , E9). (c) Modeled enrichment in ice-core $\delta^{15}\text{N}(\text{NO}_3^-)$ (E11) due to
1554 photolysis-driven loss of NO_3^- in snow compared to sub-photocatalytic zone $\delta^{15}\text{N}(\text{NO}_3^-)$
1555 observations [Erblund *et al.*, 2013, Frey *et al.*, 2009, Jarvis, 2008, Shi *et al.*, 2014, Sofen
1556 *et al.*, 2014].
1557
1558
1559
1560
1561
1562
1563
1564
1565
1566
1567
1568
1569
1570

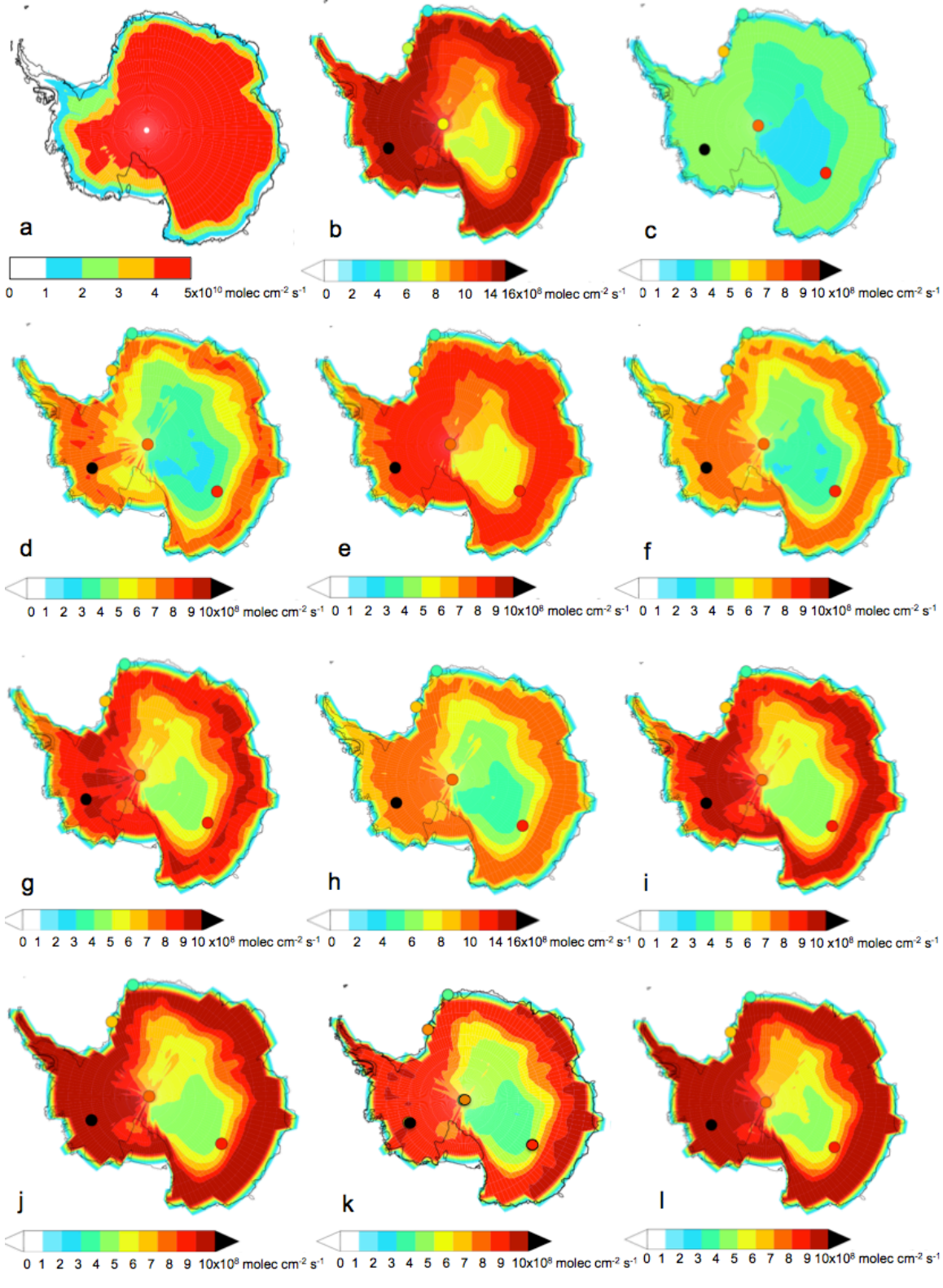


1571
 1572 Figure 10. NRF versus f values across Antarctica. (a) Regions where NO_3^- remains in the
 1573 photic zone for 3 years or less. (b) Regions where NO_3^- remains in the photic zone for
 1574 more than 3 years. The color scale represents the number of years NO_3^- remains in the
 1575 photic zone (τ_z). Note the different x-axis range for (a) and (b).

1576
 1577
 1578
 1579
 1580
 1581
 1582
 1583
 1584
 1585
 1586
 1587
 1588
 1589
 1590
 1591
 1592
 1593
 1594
 1595
 1596
 1597
 1598
 1599
 1600
 1601
 1602

1603
1604

Appendix A



1607
1608

1609 Figure 1A. Results of sensitivity studies that show how the average austral summer (DJF)
1610 flux of snow-sourced NO_x ($\overline{F_{NOx}}$) in Antarctic snowpacks is altered by changes in
1611 variables relevant to snow NO₃⁻ photolysis. The standard set of variables in the above
1612 figures are quantum yield (ϕ) = 0.002 molec photon⁻¹, fraction of photolabile NO₃⁻ (F_p) =
1613 1, annual mean sub-surface snow NO₃⁻ ($[NO_3^-]_{bot}$) = 60 ng g⁻¹, radiation equivalent mean
1614 ice grain radii (r_e) = 332 μ m, NO₃⁻ enhancement factor (EF) = 6, bulk snow extinction
1615 coefficient ($Kext_{tot}$) = 1.7x10⁻³ to 6.9x10⁻³ (spatial variability), and annual mean snow
1616 black carbon (C_{BC}) = 0.08 to 0.6 ng g⁻¹ (spatial variability). Observed $\overline{F_{NOx}}$ values are
1617 overplotted (see Figure 4 for references). In (a), for the top centimeter of snow, the Zhu et
1618 al. [2010] ϕ is applied to all dry-deposited NO₃⁻ and the Chu and Anastasio [2003] ϕ is
1619 applied to all wet-deposited NO₃⁻. Below 1 cm, the Chu and Anastasio [2003] ϕ is applied
1620 to all NO₃⁻. In (b), $[NO_3^-]_{bot}$ is doubled from the base case value and in (c), $[NO_3^-]_{bot}$ is
1621 halved from the base case value. In (d), the C_{BC} is doubled from base case values and in
1622 (e) the C_{BC} is halved from base case values. In (f), $EF=1$ and in (g), $EF=10$. In (h), $Kext_{tot}$
1623 is a factor of 1.2 higher than the base case value. In (i), $Kext_{tot}$ is a factor of 0.8 than the
1624 base case value. In (j), r_e is representative of austral mid-summer (January) conditions is
1625 used (see Table 3 footnote). In (k), r_e is representative of austral spring, fall, and winter
1626 (March-November) conditions. In (l), r_e is representative of austral early summer and
1627 late summer (December, February) conditions. Note different color scales.

1628

1629

1630

1631

1632

1633

1634

1635

1636

1637

1638

1639

1640

1641

1642

1643

1644